Solid Earth

Transient conduit permeability controlled by a shift between compactant shear and dilatant rupture at Unzen volcano (Japan)

Yan Lavallée[1,a], Takahiro Miwa[2], James D. Ashworth[1], Paul A. Wallace[1,3], Jackie E. Kendrick[1,a], Rebecca Coats[1], Anthony Lamur[1,a], Adrian Hornby[4], Kai-Uwe Hess[5], Takeshi Matsushima[6], Setsuya Nakada[7], Hiroshi Shimizu[6], Bernhard Ruthensteiner[8], and Hugh Tuffen[9]

[1]Earth, Ocean and Ecological Sciences, University of Liverpool, Liverpool, United Kingdom
[2]National Research Institute for Earth Science and Disaster Resilience (NIED),
Tsukuba, Japan
[3]Department of Geosciences, Environment and Society, Université libre de Bruxelles, Brussels, Belgium
[4]Earth and Atmospheric Sciences, Cornell University, Ithaca, NY 14850, United States of America
[5]Earth and Environmental Sciences, Ludwig Maximilian University of Munich, Munich, Germany
[6]Institute of Seismology and Volcanology, Faculty of Science, Kyushu University, Shimabara, Nagasaki, Japan
[7]National Research Institute for Earth Science and Disaster Resilience, Tennodai, Tsukuba, 305-0006, Japan
[8]Staatliche Naturwissenschaftliche Sammlungen Bayerns (SNSB), Zoologische Staatssammlung München,
Munich, Germany
[9]Lancaster Environment Centre, Lancaster University, Lancaster, United Kingdom
[a]now at: Earth and Environmental Sciences, Ludwig Maximilian University of Munich, Munich, Germany

Correspondence: Yan Lavallée (yan.lavallee@min.uni-muenchen.de)

Abstract. The permeability of magma in volcanic conduits controls the fluid flow and pore pressure development that regulates gas emissions and the style of volcanic eruptions. The architecture of the permeable porous structure is subject to changes as magma deforms and outgasses during ascent. Here, we present a high-resolution study of the permeability distribution across two conduit shear zones (marginal and central) developed in the dacitic spine that extruded towards the closing stages of the 1991–1995 eruption at Unzen volcano, Japan. The marginal shear zone is approximately 3.2 m wide and exhibits a 2 m wide, moderate shear zone with porosity and permeability similar to the conduit core, transitioning into a ~ 1 m wide, highly sheared region with relatively low porosity and permeability, as well as an outer 20 cm wide cataclastic fault zone. The low-porosity, highly sheared rock further exhibits an anisotropic permeability network, with slightly higher permeability along the shear plane (parallel to the conduit margin), and is locally overprinted by oblique dilational Riedel fractures. The central shear zone is defined by a 3 m long by ~ 9 cm wide fracture ending bluntly and bordered by a 15–40 cm wide damage zone with permeability enhanced by ~ 3 orders of magnitude; directional permeability and resultant anisotropy could not be measured from this exposure.

We interpret the permeability and porosity of the marginal shear zone to reflect the evolution of compactional (i.e. ductile) shear during ascent up to the point of rupture, which was estimated by Umakoshi et al. (2008) at ~ 500 m depth. At this point the compactional shear zone would have been locally overprinted by brittle rupture, promoting the development of a shear fault and dilational Riedel fractures during repeating phases of increased magma ascent rate, enhancing anisotropic permeability that channels fluid flow into and along the conduit margin. In contrast, we interpret the central shear zone as a shallow, late-stage dilational structure, which partially tore the core of the spine, leaving a slight permanent displacement. We explore constraints from monitored seismicity and stick-slip behaviour to evaluate the rheological controls, which accompanied the shift from compactional toward dilational shear as magma approached the surface,

and discuss their importance in controlling the permeability development of magma evolving from overall ductile to increasingly brittle behaviour during ascent and eruption.

1   Introduction

1.1   Outgassing pathways and volcanic eruptions

The style and timing of activity exhibited during a volcanic eruption are strongly influenced by the presence and mobility of volatiles in magma (Sparks, 1997; Woods and Koyaguchi, 1994) and the surrounding conduit wall rock (Jaupart and Allègre, 1991). During magma ascent, volatiles are exsolved into gas bubbles (Navon et al., 1998; Sparks, 2003) as their solubility decreases with decompression (Liu et al., 2005), crystallisation (Tait et al., 1989), and heat generated by crystallisation (Blundy et al., 2006) and shear (Lavallée et al., 2015). This causes the accumulation of pressurised fluids in vesicles that charges ascending magma, which, if sufficient, may lead to fragmentation (Mueller et al., 2008; Alidibirov and Dingwell, 1996) and an explosive eruption (Sahagian, 1999). The development of a permeable network governs outgassing (Edmonds et al., 2003), pore pressure release (Mueller et al., 2005), and eruptive cyclicity (Michaut et al., 2013), thereby reducing the potential for explosive activity (Klug and Cashman, 1996) and encouraging effusion (Edmonds and Herd, 2007; Eichelberger et al., 1986; Degruyter et al., 2012). Lava dome eruptions – the topic of this study – commonly switch between effusive and explosive modes of activity due to this competition between permeability, pore fluid pressure, and the structural integrity of magma (Melnik and Sparks, 1999; Calder et al., 2015; Cashman and Blundy, 2000; Castro and Gardner, 2008; Edmonds et al., 2003; Lavallée et al., 2013, 2012; Sparks, 1997; Holland et al., 2011; Kendrick et al., 2016; Platz et al., 2012). Considering the water solubility–pressure relationships (Zhang, 1999), permeability–porosity relationships in magma (Westrich and Eichelberger, 1994), and eruptive patterns (Edmonds et al., 2003), it has been suggested that much of the outgassing during lava dome eruptions occurs in the upper few kilometres of the conduit (Westrich and Eichelberger, 1994; Edmonds et al., 2003). This observation is corroborated by rapid shallowing of seismicity leading to explosions (e.g. Rohnacher et al., 2021), and the existence of shallow long-period seismic signals resulting from resonance in fractures and faults (Chouet, 1996; Matoza and Chouet, 2010) as fluids are channelled to the surface (Holland et al., 2011; Kendrick et al., 2016; Gaunt et al., 2014; Nakada et al., 1995; Newhall and Melson, 1983; Pallister et al., 2013b; Sahetapy-Engel and Harris, 2009; Sparks, 1997; Sparks et al., 2000; Edmonds et al., 2003; Varley and Taran, 2003; Stix et al., 2003). Therefore, understanding the evolution of the permeable network during eruptive shearing is

central to constraining the evolution of magmatic systems in the shallow crust (Blower, 2001).

Close examination of the architecture of shallow dissected conduits and structures in vent-proximal silicic lavas exposes complex shearing histories that would impact the permeable porous network of erupting magma. These structures reveal porosity contrasts through the lavas, and strain localisation near the conduit margins is commonly identified via the presence of flow bands and variably porous shear zones with a spectrum of configurations (Gaunt et al., 2014; Kendrick et al., 2012; Kennedy and Russell, 2012; Pallister et al., 2013a; Smith et al., 2001; Stasiuk et al., 1996; Tuffen and Dingwell, 2005); these are features that are preserved to differing extents in crystal-poor and crystal-rich magmas (Calder et al., 2015; Lavallée and Kendrick, 2021). For example, crystal-poor obsidian in dissected conduits and dykes commonly exhibits marginal flow bands, showing alternation between glassy, finely crystalline, and microporous bands (Gonnermann and Manga, 2007). Flow bands also occur as variably sintered, cataclastic breccia layers, resulting from fracture and healing cycles (Tuffen and Dingwell, 2005; Tuffen et al., 2003), and as variably sintered tuffisite layers, resulting from fragmentation and entrapment of fragments into narrow fractures (Castro et al., 2012; Heiken et al., 1988; Kendrick et al., 2016; Kolzenburg et al., 2012). Exposed crystal-poor conduits, dykes, and domes are commonly dense, as the porous network may easily collapse (unlike crystal-rich lavas; e.g. Ashwell et al., 2015). The collapse of the porous network occurs as eruptions wane and pore pressure is insufficient to counteract surface tension as well as local magmastatic and lithostatic stresses (Kennedy et al., 2016; Wadsworth et al., 2016), a process which hinders interpretation of the syn-eruptive permeable structure of crystal-poor magma from the study of large-scale relict formations. Studies of erupted crystal-poor pumices (which quench rapidly) help provide constraints on the extent of magma permeability at the point of fragmentation (Wright et al., 2006), but the task of reconstructing the permeable architecture of an entire conduit from these pyroclasts is challenging (Dingwell et al., 2016) and further complicated by post-fragmentation vesiculation (Browning et al., 2020) as well as vesicle relaxation (Rust and Manga, 2002), and it therefore remains to be attempted systematically.

Crystal-rich volcanic rocks (the subject of this study) expose a wider range of permeable porous structures (Farquharson et al., 2015; Mueller et al., 2005; Klug and Cashman, 1996; Lamur et al., 2017; Kushnir et al., 2016; Ryan et al., 2020; Kendrick et al., 2021). These rocks frequently share common characteristics and evidence that crystal-rich magmas preferentially shear and accumulate damage near the conduit margins, defined by flow bands and/or cataclastic fault zones, adjacent to brecciated wall rocks (Sparks et al., 2000; Hale and Wadge, 2008; Watts et al., 2002). For instance, dacitic volcanic spines extruded in 2004–2008 at Mount St. Helens (USA) and in 1994–1995 at Unzen vol-

cano (Japan) reveal the presence of a complex "damage halo" near the conduit margin (Calder et al., 2015; Gaunt et al., 2014; Pallister et al., 2013a; Smith et al., 2001; Kendrick et al., 2012; Wallace et al., 2019). Shear zones at Mount St. Helens (Gaunt et al., 2014) and at Chaos Crags, Lassen volcano (Ryan et al., 2020), showed increased porosity and permeability, as well as the development of permeability anisotropy towards the conduit margin, thus describing scenarios in which shearing of dense, crystal-rich magma induced dilation. In the case of Mount St. Helens, in the later Spine 7, the fault zone is defined by the presence of a pseudotachylyte (Kendrick et al., 2012), a feature which can reduce the permeability of shear zones in magmas (Kendrick et al., 2014a). At Unzen volcano, Smith et al. (2001) qualitatively described the character of the shear zone developed in the centre of the lava spine at Mount Unzen, highlighting the presence of a dilational cavity associated with shearing in the core of the magmatic column. However, they did not quantify any porosity–permeability relationships. The cavity (hereafter termed "central shear zone") was defined by an area in which the groundmass was torn, producing pore spaces in the shadow of phenocrysts. The margin of the Unzen spine also hosts a spectrum of shear textures (Hornby et al., 2015; Wallace et al., 2019), and significant low-frequency seismicity during the eruption indicated flushing of fluids in the marginal fault zone (Lamb et al., 2015). Thus, the study of evolving monitored signals and eruptive products at Unzen depicts a wide range of outgassing pathways, which evolve during the course of magma ascent and lava dome eruptions.

1.2 The permeability of magmas and rocks

Several studies have explored the permeability evolution of volcanic materials, but due to the occurrence of many influential structural and petrological processes in shallow volcanic conduits, no solutions yet encompass the complete history of magma permeability during volcanic eruptions, especially its time- and strain-dependent evolution. Following nucleation and growth, bubbles interact and coalesce beyond a certain vesicularity, termed the percolation threshold, promoting the onset of fluid flow through a connected bubble network (Baker et al., 2012; Eichelberger et al., 1986; Rust and Cashman, 2004; Burgisser et al., 2017). The porosity of the percolation threshold varies widely (between ∼ 30 vol % and 78 vol % bubbles) depending on the size and geometry distributions of the bubble population (Colombier et al., 2017; Rust and Cashman, 2004; Burgisser et al., 2017). Vesiculation experiments have shown that permeability remains low in isotropically vesiculated (aphyric and crystal-bearing) magmas as percolation initiates at vesicularities higher than those theoretically predicted (Okumura et al., 2012, 2009). Yet, bubble coalescence may be accentuated by transport processes such as the thinning or draining of melt along the bubble wall (Castro et al., 2012), deformation (Ashwell et al., 2015; Kennedy et al., 2016; Okumura

et al., 2010, 2006, 2008; Wadsworth et al., 2017; Shields et al., 2014; Farquharson et al., 2016b; Kendrick et al., 2013), and rupture (Lamur et al., 2017; Lavallée et al., 2013; Heap and Kennedy, 2016; Okumura and Sasaki, 2014; Heap et al., 2015a; Laumonier et al., 2011), or it may be lessened by fracture infill (Kendrick et al., 2014a, 2016; Wadsworth et al., 2016), all of which influence the permeability of magma and promote permeability anisotropy (Farquharson et al., 2016c) during its prolonged ascent to the Earth's surface.

In recent decades, laboratory measurements have helped us gain a first-order constraint on the permeability–porosity relationships of volcanic products (Eggertsson et al., 2020; Mueller et al., 2005; Acocella, 2010; Rust and Cashman, 2011; Colombier et al., 2017; Farquharson et al., 2015; Klug and Cashman, 1996). These suggest a nonlinear increase in permeability with porosity; yet, depending on the nature of the porous network as influenced by eruptive history, the permeability of rocks with a given porosity may vary by up to 4–5 orders of magnitude. Controlled laboratory experiments have given us insights on probable permeability trends of magma subjected to different stress, strain, and temperature conditions (Ashwell et al., 2015; Kendrick et al., 2013; Lavallée et al., 2013; Okumura et al., 2012, 2006; Shields et al., 2014), but a complete description of the dynamic permeability of deforming magma requires in operando determination under controlled conditions, which remain scarce (Gaunt et al., 2016; Kushnir et al., 2017b; Wadsworth et al., 2017, 2021); studies have shown that surface tension and/or low-strain-rate conditions under positive effective pressure (i.e. confining pressure greater than pore pressure) promote compaction and reduce permeability. These informative descriptions require further inputs to enable robust relationships with magma rheology as influenced by the presence and configuration of bubbles. Shallow magmas contain bubbles and crystals and exhibit a non-Newtonian rheology (Caricchi et al., 2007; Lavallée et al., 2007; Lejeune et al., 1999; Lejeune and Richet, 1995; Kendrick et al., 2013; Coats et al., 2018) that favours the development of strain localisation, in particular by preferentially deforming pore space (Kendrick et al., 2013; Okumura et al., 2010; Shields et al., 2014; Pistone et al., 2012; Mader et al., 2013). As magma shears, the porous network adopts a new configuration reflecting the stress conditions and magma viscosity (Rust et al., 2003; Wright and Weinberg, 2009), which influences the permeability (Ashwell et al., 2015; Kendrick et al., 2013; Okumura et al., 2010, 2009, 2006, 2008, 2013). Shearing may increase or decrease the permeability depending on the applied stress, strain and porosity of the deforming material, and direction of the permeability measurement due to the development of anisotropy (Ashwell et al., 2015; Kendrick et al., 2013). In cases of extreme shear, magma may rupture, thereby increasing pore connectivity and permeability (Laumonier et al., 2011; Lavallée et al., 2013; Okumura et al., 2013) until the fracture heals via diffusion (Okumura and Sasaki, 2014; Tuffen et al., 2003; Lamur et al., 2019;

Yoshimura and Nakamura, 2010), seals via secondary mineralisation (Heap et al., 2019; Ball et al., 2015), or infills with tuffisitic material (Castro et al., 2012; Kendrick et al., 2016; Kolzenburg et al., 2012; Tuffen and Dingwell, 2005), which may densify through time (Kendrick et al., 2016; Vasseur et al., 2013; Wadsworth et al., 2014; Farquharson et al., 2017). The densification of magma under isotropic stresses (due to surface tension) has been reconstructed using high-resolution X-ray computed tomography from synchrotron imaging, providing us with a first complete description of magma permeability evolution as a function of porosity. This indicates that densification intrinsically relates to the evolution of the size distribution and surface area of the connected pore space (Wadsworth et al., 2017, 2021). Nonetheless, a time- and strain-dependent description of the development of the porous network of shearing magma remains incomplete, and information must be sourced from our understanding of permeability evolution in deforming rocks.

In rock physics, the evolution of the porous network in deforming rocks has been extensively studied. In its simplest description, the modes of deformation differ at low and high effective pressures as rocks adopt brittle or ductile behaviour, respectively. These are defined as a macroscopic behaviour (not a mechanistic description), whereby "brittle" refers to the localisation of deformation leading to rupture, and "ductile" refers to the inability for rocks to localise strain during deformation (e.g. Rutter, 1986); see Lavallée and Kendrick (2020) and Heap and Violay (2021) for reviews of brittle and ductile deformation in volcanic materials. The key distinction between these two deformation modes is that brittle failure generally results in local dilation (i.e. the creation of porosity), whereas ductile deformation results in compaction of the porous network (Heap et al., 2015a). As a result, brittle (dilational) failure generally enhances the permeability of rocks (Heap and Kennedy, 2016; Lamur et al., 2017; Farquharson et al., 2016b), whereas ductile (compactional) deformation generally causes reduction in permeability (Heap et al., 2015a; Loaiza et al., 2012), though there are exceptions. Despite its crucial role in defining deformation mode in rock, the role of effective pressure in dictating the ductile and brittle modes of deformation has not been systematically mapped out for multiphase magmas; instead, we generally consider the effects of temperature and applied stress or strain rate (e.g. Lavallée et al., 2008) over that of stress distribution, as the deformability of magma imparts technical challenges to classic rock mechanics tests and permeability determinations (Kushnir et al., 2017b). We may thus anticipate some similarities between rock and magma deformation modes, whereby at high effective pressure, ductile deformation is favoured via compactant viscous flow or even cataclastic flow (if strain rates are high enough to cause pervasive fracturing of bubble walls), causing porosity and permeability reduction; at low effective pressure, viscous flow may promote compaction at low strain rates, whereas dilation may ensue if strain rate favours localised rupture

(Lavallée and Kendrick, 2020). Similarly, embrittlement may take place if a porous magma efficiently compacts, shifting its properties from the ductile to brittle regime (Heap et al., 2015a). Across this viscous–brittle transition, magma rupture may be partial and end abruptly, leaving a blunt fracture tip (Hornby et al., 2019). Most, if not all, of the features observed in experimentally deformed rocks and lavas should be observable in shallow magmatic systems, hinging on a delicate balance between ductile and brittle deformation regimes; these would influence outgassing, prompting temporal and spatial variations in effective pressure. In this study, we examine the well-preserved, dacitic lava spine erupted in 1994–1995 at Unzen volcano to constrain the permeability of dilational and compactional shear zones that developed in the shallow volcanic conduit.

1.3 1990–1995 eruption of Unzen volcano

Unzen volcano is a stratovolcano located near the city of Shimabara on the island of Kyushu, Japan (Fig. 1). The volcano underwent a 5-year period of protracted dome growth, which threatened the surrounding population with the occurrence of several thousand rockfalls and many pyroclastic flows, such as the destructive event on 3 June 1991 that caused 43 fatalities. Activity initiated in early 1990 with a series of phreatic explosions and brief extrusion of a spine on 19 May; this was swiftly followed by continuous growth of a lava dome until early 1995 (Nakada et al., 1995). Between October 1994 and January 1995, the eruption concluded with the extrusion of a spine through the dome surface (Fig. 1c). At the dome surface, gas emissions focused along the spine-marginal faults (Ohba et al., 2008). The dome products have a dacitic composition and contain euhedral phenocrysts of plagioclase, amphibole, and biotite in a groundmass containing microlites of plagioclase, amphibole, pyroxene, and iron oxides (Nakada et al., 1995; Wallace et al., 2019). Petrological constraints suggest that degassing initiated at a pressure of approximately 70–100 MPa, i.e. in the upper ~ 3–4 km depth (Nakada et al., 1995).

Dome growth occurred in stages, forming 13 discrete lobes until mid-July 1994. Growth was observed to be typically exogenous when effusion rates were high and endogenous at effusion rates lower than $2.0 \times 10^5 \, \mathrm{m^3 \, d^{-1}}$ (Nakada et al., 1999). In 5 years, the eruption generated $2.1 \times 10^8 \, \mathrm{m^3}$ of lava at an average ascent rate estimated at 13–20 m d^{-1} (Nakada et al., 1995); the final spine extruded from late 1994 to early 1995 at a rate of approximately 0.8 m d^{-1} (Yamashina et al., 1999). The rheology of the erupted dome lavas has been a source of debate (Goto et al., 2020; Sato et al., 2021), as it is challenging to precisely reconstruct the physico-chemical, petrological, and structural parameters which control rheology as a function of depth during eruptions. For the late-stage spine, Nakada and Motomura (1999) proposed that it formed due to a lower effusion rate, which resulted in extensive magma degassing and crystallisation and thus high viscosity,
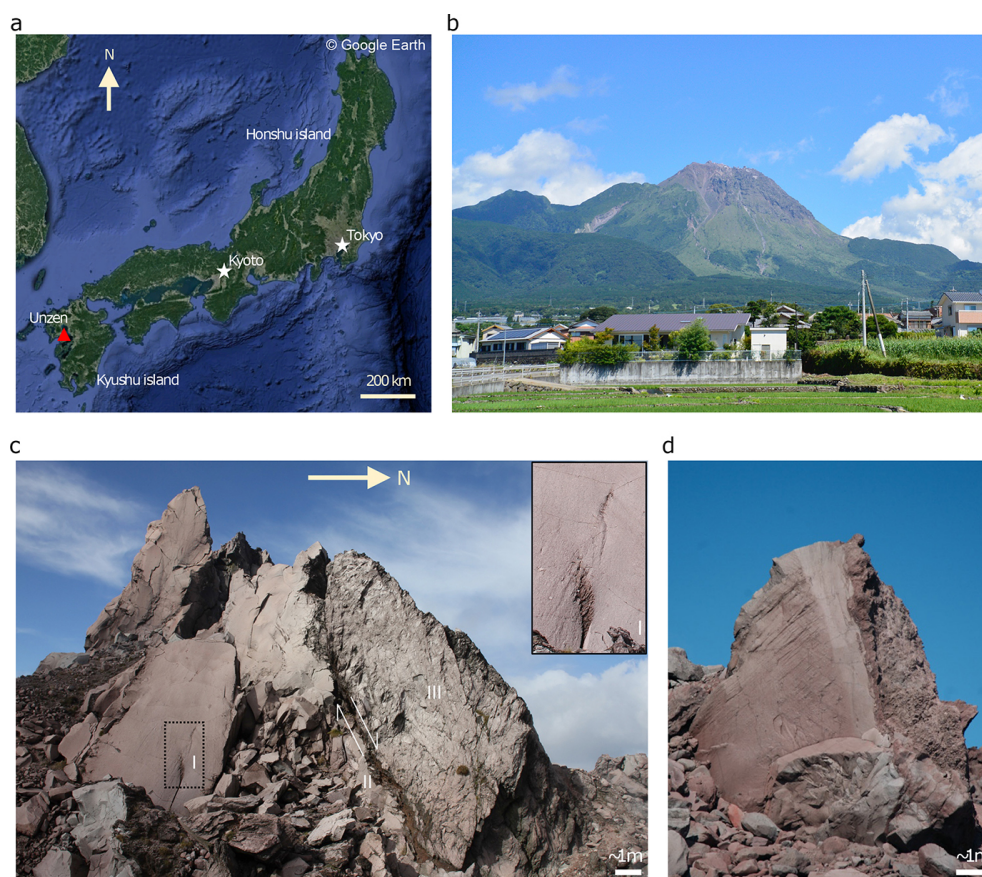
Figure 1. (a) © Google Earth image showing the location of Unzen volcano on the island of Kyushu, Japan. **(b)** Photograph of Unzen volcano, looking northwest, viewed from near Onokoba in the suburbs of Shimabara city. **(c)** Photo of the relict 1994–1995 spine at Unzen volcano (looking westward), showing (I) the central shear zone (i.e. the cavitation structures detailed in Smith et al., 2001, further expanded in the inset), (II) the marginal shear zone bordered by a fault (dark orange–brown colour), and (III) a large block of sintered breccia of earlier domes, which has become welded to the fault material and extruded with the spine. Adapted from Hornby et al. (2015). **(d)** Photograph of a fragment of the spine showing the primary internal structure of the shear zone, bordered by a set of closely spaced, inclined fractures to the left and indurated breccia to the right.

which promoted rupture and exogenic growth at relatively low strain rates (e.g. Hale and Wadge, 2008; Goto, 1999). Extrusion occurred through pulsatory magma ascent, accompanied by ~40 h inflation–deflation cycles (Yamashina et al., 1999) and a rhythmic pattern of summit earthquakes, interpreted to result from magma rupture in the top 0.5 km of the conduit (Lamb et al., 2015; Umakoshi et al., 2008); waveform correlation of the seismic record revealed rhythmic seismicity grouped into two primary clusters (Lamb et al., 2015). Hornby et al. (2015) statistically analysed the slip duration of seismic events in the clusters, defining a mode and mean of 0.1 s. As magma ascent occurred through an inclined conduit (Umakoshi et al., 2008), the spine extruded at an angle of ~45° towards the ESE (Fig. 2a) and increasingly leaned against the lower fault zone as extrusion rate waned, causing the shallowing of seismogenic magma rupture in this area (Lamb et al., 2015). In contrast, the upper fault zones may have opened up as the spine settled, thus triggering rup-

ture at increasing depth and promoting preferential pathways for fluid flow (Lamb et al., 2015). By the end of the eruption, the spine achieved approximate dimensions of 150 m length, 30 m width, and 60 m height (Nakada and Motomura, 1999; Nakada et al., 1999); it is complemented by multiple fragments of spines, extruded earlier in the eruptive phase, which we examine in this study. Unfortunately, the lower and upper fault zones are not observable in the spine exposures, but the northern lateral conduit margin contains well-defined shear zones (Smith, 2002; Smith et al., 2001), which are revisited here and augmented by structural and microtextural descriptions as well as porosity and permeability constraints. Our study of the spine sheds new light on the permeability evolution of its shear zones and thus the nature of outgassing during the waning phase of the 1990–1995 eruption.
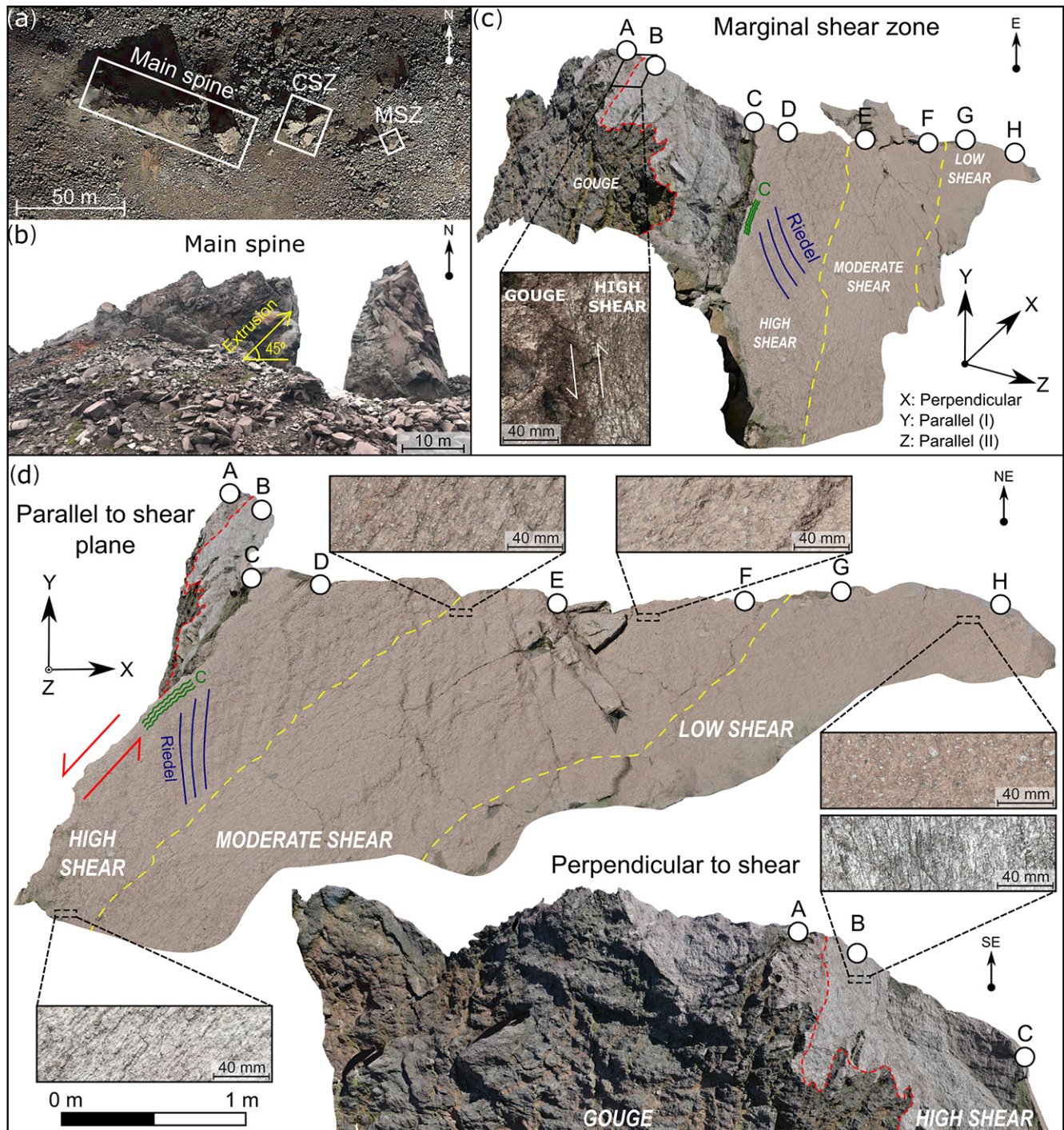
Figure 2. Location of the lava spine blocks and characteristics of the marginal shear zone. **(a)** An aerial view of Unzen lava dome summit showing the remnants of the 1994–1995 lava spine, including the main spine, the central shear zone (CSZ) block, and the marginal shear zone (MSZ) block. **(b)** Photograph of the main spine inclined towards the east. **(c)** 3D construction of the marginal shear zone block (created using the photogrammetry 3DF Zephyr by 3Dflow). The outcrop is annotated to show the location of samples (A–H) as well as the four main regions (gouge as well as high, moderate, and low shear zones) and key features, including the fault contact (red dashed curve), shear zone transitions (yellow dashed curves), extension of tensile fractures (C; green lines), and Riedel fractures (blue curves). The inset shows details of the fault plane, dividing the gouge and high shear zone. **(d)** View of the MSZ block parallel to the shear plane and perpendicular to the shear plane. Insets show surface textures across the shear zone. Directional arrows X, Y, and Z show the orientation of sample coring relative to the shear plane.

2 Materials and methods

2.1 Localities and sample collection

The 1994–1995 lava spine was investigated during two field campaigns in November 2013 and May 2016. Close structural examination at different scales forms the basis of this study along with porosity and permeability measurements using field and laboratory equipment. Owing to the inclination of the spine (extruded towards the east), large blocks ranging from 5 to 20 m wide are dislocated from the front of the in situ western main spine structure (Fig. 2a, b). Here, we investigated two blocks that reveal a central shear zone (CSZ) and marginal shear zone (MSZ) that developed in the spine. These detached, yet fully intact, spine blocks were selected owing to their contrasting shear textures that would have represented different positions within the volcanic conduit during magma ascent and extrusion (i.e. central vs. marginal), thus allowing assessment of syn-eruptive outgassing pathways. The marginal shear zone (MSZ) block, located ∼ 60 m east of the main spine (latitude: 32.76131°, longitude: 130.29983°), was carefully sampled to quantify the spatial distribution of permeability across the spine margin (samples A–H; Fig. 2c). The CSZ block, located centrally between the main spine and MSZ (latitude: 32.761271°, longitude: 130.299472°), features the dilatational cavity (described in Smith et al., 2001) and was also studied in situ using non-destructive methods to preserve the integrity of this exemplary feature. The main spine and CSZ are protected by UNESCO heritage site regulations (Figs. 1c, 2a), thus only permitting in situ sample collection from the MSZ.

2.2 Sample preparation

Samples collected from the marginal shear zone were cut and cored parallel to the shear direction and perpendicular to the shear plane in order to constrain the anisotropy developed in shear zones. A total of eight thin sections (fluorescent dyed) were prepared for microtextural analysis (labelled A–H). For the largest samples (A, B, C, E, H; see Fig. 2c–d) a set of two to three cylindrical cores (two parallel and one perpendicular to shear plane) was prepared with a diameter of 26 mm and a length of 30 or 13 mm, depending on the size of the sample. Within the highly sheared sample B (Fig. 2c–d), which is directly adjacent to the fault and gouge zone, multiple sets of cores of 20 mm diameter were prepared, closely spaced, to obtain porosity and permeability determinations at a higher resolution across this defining part of the shear zone.

2.3 Microstructural analysis in 2D and 3D

Two-dimensional (2D) analysis of the microstructures exhibited across the shear zones was carried out using a Leica DM2500P optical microscope in plane-polarised and ultraviolet (UV) light, as well as a Philips XL30 scanning electron microscope (SEM) in backscattered electron (BSE) mode,

set at 20 kV and 10 mm working distance. For this purpose, representative features were imaged for each sample across the shear zone (Fig. 3).

To further evaluate the architecture of the porous network in three dimensions (3D), four samples collected across the shear zone were scanned using a Phoenix Nanotom®M X-ray computed tomography scanner to produce high-resolution reconstructions with a voxel size of 11.111 µm. For each sample we acquired 1440 radiographs, scanning 360°, under the following conditions: exposure time of 1000 ms, voltage of 80 kV, current of 120 µA, and 0.2 mm aluminium filter. The radiographs were then reconstructed using the inverse Radon transformation (Radon, 1986), resulting in a 3D image of the sample. These files were processed in FEI Avizo and ImageJ/Fiji software to illuminate the permeable, porous network.

2.4 Porosity measurement in the laboratory

Each core was dried in an oven at 50 °C overnight, then kept in a desiccator (for thermal equilibration to ambient conditions) before being weighed and loaded in a pycnometer. The fraction of connected pores (which controls permeability; Colombier et al., 2017) was determined using a Micromeritics AccuPyc II 1340 helium pycnometer. The porosity determination first necessitated measurement of the geometric volume of the sample (V_{sample}). Then, once inserted in the specimen chamber of the pycnometer, helium gas was injected in the chamber to estimate the volume taken up by the solid fraction of the sample, thus providing the skeletal volume ($V_{skeletal}$) of the rock. The fraction of connected pores ($\phi_{connected}$) in a sample was then calculated via

$$\phi_{connected} = \frac{\left(V_{sample} - V_{skeletal}\right)}{V_{sample}}. \tag{1}$$

2.5 Permeability determination in the laboratory

The prepared cores were jacketed with a Viton™ tube and inserted in a hydrostatic cell from Sanchez Technologies to measure permeability and pore volume as a function of pressure. The jacketed samples were externally loaded using a Maximator® oil pump to various confining pressures (P_c) and internally loaded using distilled water to an average pore pressure (P_p) of 1.25 MPa in order to obtain a range of effective pressures ($P_{eff} = P_c - P_p$) from 5 to 100 MPa. Each time the sample was loaded to a new confining pressure increment, the volume of water expelled from the void space in a given sample (due to compaction) was monitored to constrain pore volume change due to crack closure as a function of pressure (Lamur et al., 2017); this allowed us to monitor when the samples (i.e. their microstructure) had equilibrated to the set conditions at each pressure step. Steady-state flow permeability (k) was then measured by applying low pore pressure gradients (ΔP) of 0.5 and 1.5 MPa to ensure laminar flow with no-slip conditions (after Heap et al., 2017a) to
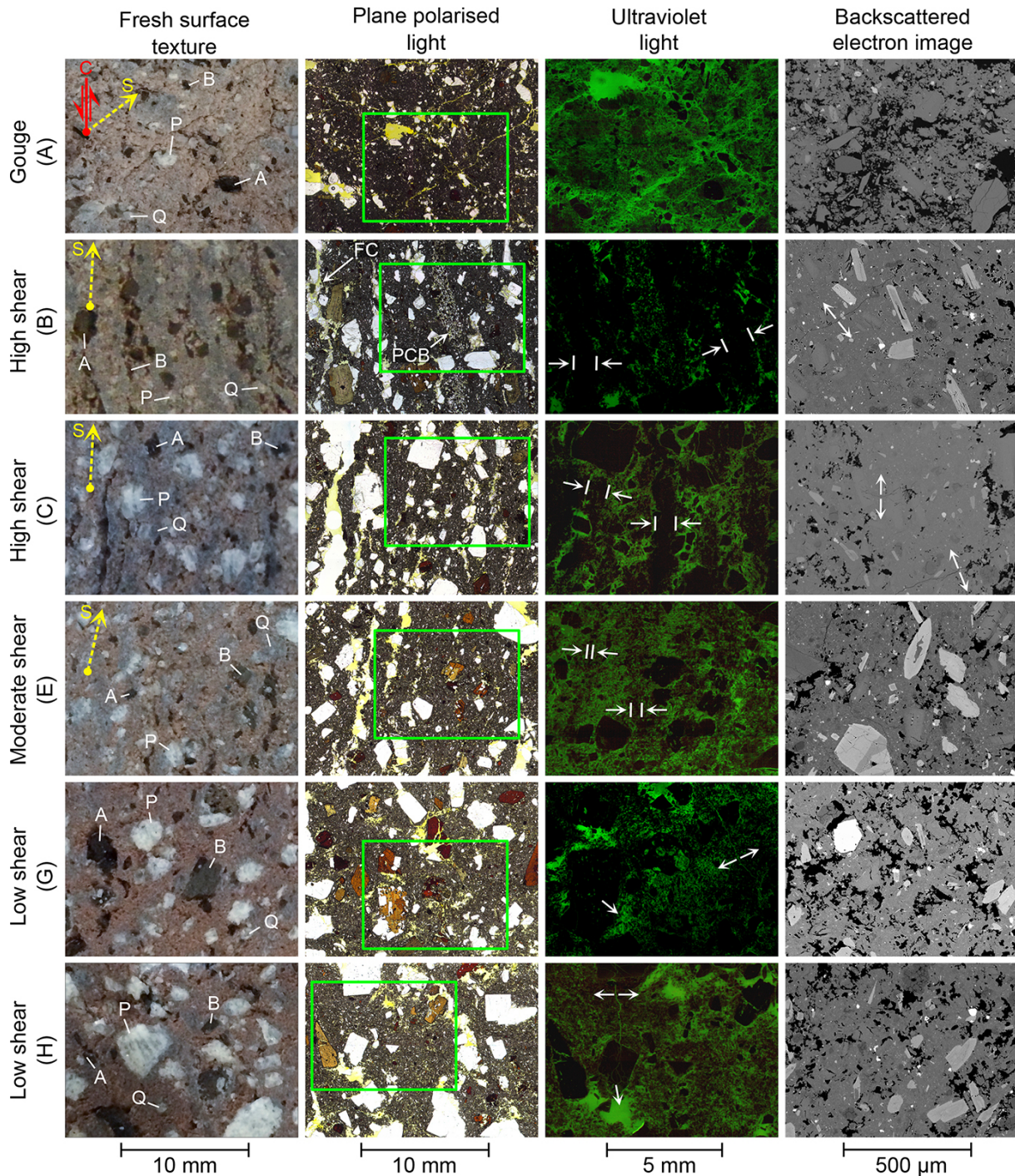
Figure 3. Composite figure of the microtextural characteristics across the marginal shear zone consisting of a photograph of fresh surface textures, plane-polarised light (PPL) photomicrographs, ultraviolet (UV) light photomicrographs, and backscattered electron (BSE) images of the groundmass. Images of the fresh surface were taken following cutting the sample perpendicular to shear. The C fabric (red line) and S fabrics (dashed yellow line) are labelled in gouge, high shear, and moderate shear zones. The C fabric runs consistently parallel to the shear direction, while the S fabric is slightly inclined to variable degrees across the MSZ. Phenocrysts observed include plagioclase (P), amphibole (A), biotite (B), and quartz (Q). Green boxes on PPL photomicrographs show the location of the UV light images, which highlight the pore structures across the MSZ. On UV light images, two white arrows pointing away from each other show the location of fractures within the groundmass (samples G and H), single arrows point to large pores adjacent to large phenocryst (samples G and H), and two arrows pointing towards each other show compaction bands (their spacing represents the width of each band; samples B and C). In the BSE images, a porous diktytaxitic texture is prevalent across the shear zone, although in the high shear zones (samples B and C) these textures are impeded by low-porosity compaction bands that show strong crystal alignment, fractured crystals (FCs), and pulverised crystal bands (PCBs).

satisfy Darcy's law:

$$k = \frac{Q\eta L}{A(\Delta P)}, \qquad (2)$$

where Q is the flow rate monitored through the sample ($m^3 s^{-1}$), η is the viscosity of the water in pores (Pa s), L is the length of the sample (m), and A is the cross-sectional area of the sample (m^2).

2.6 In situ permeability measurements in the field

To measure the permeability of rocks in the central shear zone (CSZ; Fig. 1c) that could not be sampled for laboratory testing due to preservation restrictions, we used a non-destructive, portable air permeameter (TinyPerm II) from New England Research, which estimates permeability by monitoring pressure recovery rate from a vacuum based on the concept of transient pulse permeability (Brace et al., 1968). The apparatus is handheld and needs to be employed carefully to maintain a consistent seal between the nozzle of the permeameter and rock surface throughout the measurements (lasting up to a few tens of minutes). It may be used to determine the permeability of rocks between approximately 10^{-12} and $10^{-16} \, m^2$ (Farquharson et al., 2015; Kendrick et al., 2016; Lamur et al., 2017). In this study, three transects were measured across the central shear zone, and all measurements were performed twice to ensure precision of the method (as determined in Lamur et al., 2017).

3 Observations and results

The 1994–1995 spine structure at Mount Unzen is exposed in several large, segmented blocks (Figs. 1c–d; 2a–b). A thorough structural description of the main spine structure and subsidiary block (e.g. CSZ) can be found in Smith et al. (2001); here we highlight the main features. The lava spine is split into a few very large primary blocks ~ 20–30 m wide and high (Figs. 1c–d, 2a–b), broken roughly perpendicular to extrusion direction: westward and inclined (see Fig. 2b). The CSZ block seen in Fig. 1c shows a > 8 m wide variably deformed core (I) lying adjacent to a 2 m wide intensely sheared zone (II), bordered to the north by a dextral fault and coupled to a large, indurated breccia (III), uplifted from the surrounding dome. The lower and southern edges were not exposed. The upper edge of the spine was not accessible, but we noted large, incoherent brecciated blocks. The rear of this outcrop as well as the main in situ spine structure exhibit irregular, metre-scale polygonal joints, although these are not developed in the face of the outcrop studied here (Fig. 1c). Additional fragments of the spine occur in a few subsidiary blocks (e.g. Fig. 1d), located a few tens of metres to the east of the main spine (Fig. 2a). These blocks, which were emplaced prior to the main spine, expose several sections through the spine and reveal the evolving architecture of the shear zone in the shallow magmatic conduit. One

such block, shown in Fig. 1d, exhibits a ~ 1 m wide shear zone bordered to the left by a set of oblique tensile fractures, reaching 2–5 m in length and spaced at ~ 3 to ~ 10 cm intervals, and to the right by an indurated breccia. This prominent block was not sampled or further studied to preserve its integrity.

3.1 The marginal shear zone

3.1.1 Structural and microtextural observations

Our primary field location for this study was a 4.7 m wide block of the spine, exposing the northern marginal shear zone consisting of gouge, sheared lava and the spine core (Fig. 2c–d). The outcrop displayed mild surface weathering in the form of a thin (micrometre size) veneer of unknown precipitate on the rock surface (which was inclined at an angle of ca. 40° towards the west). This thin veneer did not visually obstruct any primary magmatic textures and structures, and the shear texture was clearly visible, yet we determined that it would prevent accurate field permeability constraints. Four distinct degrees of shear were visually defined through textural examination and changes in surface roughness across this section of the conduit (Fig. 2c–d): a fault gouge zone (sample A) bordering a high shear zone (samples B, C, D), a moderate shear zone (samples E, F), and a low shear spine core (samples G, H) in decreasing order of surface roughness and visually observable fracture density variations; quantitation of fracture density was not attempted as we deemed the thin veneer may have prevented meaningful accuracy. This shear-based division is consistent with a complementary investigation of the mineralogical characteristics of this shear zone (Wallace et al., 2019). The contacts between shear zones trend approximately E–W in the outcrop (Fig. 2c, d) and therefore roughly parallel to the spine emplacement direction to the ENE, despite the detachment of this spine block from the main intact spine body to the west. Eight samples were systematically collected across this shear zone for further analysis (labelled A–G in Fig. 2c, d): eight for 2D microstructural analysis (PPL, UV light, and BSE imagery; Fig. 3), four for tomographic imaging (Fig. 4), and five for porosity and permeability determination (Fig. 5–6). (Note that multiple cores were obtained from the five blocks sampled for laboratory measurements.)

The spine core, termed low shear herein (~ 1.5 m wide; Fig. 2c, d), exhibited a smooth surface and the phenocrysts showed no preferred orientation at the macroscopic scale. In samples G and H collected from the low shear zone (Fig. 3), phenocrysts of plagioclase, amphibole, and biotite (plus minor quartz) are typically euhedral, largely intact, and up to ~ 5 mm in length (Fig. 3); groundmass microlites also show no preferred orientation in BSE images. The porous structure is characterised by a diktytaxitic texture composed of some large, irregular vesicles with "ragged" edges, appearing intrinsically related to the presence of surrounding phenocrysts
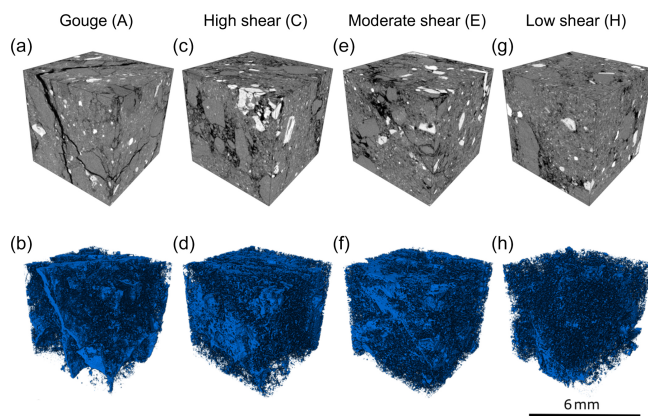
Gouge (A) High shear (C) Moderate shear (E) Low shear (H)

Figure 4. Tomographic reconstructions of four samples across the shear zones: **(a–b)** A, **(c–d)** C, **(e–f)** E, **(g–h)** H. The upper row shows density-based images of tomographic reconstructions, whereas the lower row highlights the porous network in blue, and the solid fraction is transparent. The reconstructions show that the porous fraction becomes increasingly localised towards the fault plane (i.e. from right to left).

(single white arrows on UV light images in Fig. 3). Small fractures are often seen to originate from these large vesicles, penetrating pervasively through both phenocrysts and the groundmass (double white arrows in Fig. 3). The groundmass contains abundant small vesicles, showing a high degree of connectivity as revealed by tomography (Fig. 4g–h).

The moderate shear zone is approximately 2 m wide (Fig. 2c, d). In this zone, we observed an increased fracturing of phenocrysts and changes in the distribution of porosity. Scrutinising sample E via microscopy, we observe that the phenocrysts, which rarely exceed 2 mm in size in this zone, are commonly micro-fractured (Fig. 3). The vesicles are occasionally large (3 mm) and connected (Figs. 3, 4e–f), and while the vesicular texture remains diktytaxitic (as in the low shear spine core), the vesicles in sample E appear increasingly aligned and localised around phenocrysts as the magnitude of shear increases towards the fault; similarly, the microlites show increasing degrees of alignment (revealed by undulose extinction angles; see Wallace et al., 2019). Thin bands (< 200 μm width) of reduced porosity are observed to localise in the groundmass (see facing double arrows in UV light images in Fig. 3), which are notably absent in the low shear zone; these are (sub-)parallel to the shear plane. The tomographic reconstructions show irregular vesicles, which are surrounded by fractures and invaded by rock fragments (Fig. 4e). These vesicles enhance the connectivity of the porous network (Fig. 4f).

The high shear zone is approximately 1 m wide (Fig. 2c, d) and marks the beginning of microscopic and mesoscopic shear bands at a scale of the order of a few millimetres nearly parallel to the direction of shear; these increase in abundance and scale nearer the fault, especially within the final 0.1–0.2 m (see features denoted in Fig. 2c–d as well as en-

larged in the inset). The bands, which form a pervasive foliation (S), consist of elongate, white porphyritic plagioclase lenses that are fractured and crenulated. The C–S fabrics are parallel in this area. These porphyritic bands are flanked by reddish-brown groundmass as well as thin, elongate biotite phenocrysts (see sample B "fresh surface" in Fig. 3). The plagioclase and biotite commonly exhibit a mineral fish texture. Under the microscope, we observe that the biotite shows undulose extinction from crystal–plastic deformation (see Wallace et al., 2019, for a detailed crystal plasticity study). Intense banding (observed as faint lineations of reduced porosity under UV light in the moderate shear zone; Fig. 3) is observed adjacent to, and running parallel to, the fault–gouge contact. The bands are up to ∼ 1 mm wide and display variations in porosity under UV light (Fig. 3), as also revealed by tomography (Fig. 4c–d). The dense bands are traversed by hairline fractures a few hundred micrometres in length and contain a few isolated vesicles (70 μm), generally adjacent to large phenocryst fragments (samples B and C in Fig. 3). More porous bands display disordered and fragmental textures (sample B), with abundant, irregular large pores and cracks, as well as pulverised phenocrysts (PPL and UV light in Fig. 3); macroscopically, the most porous bands often appear as ragged tensile fractures. The transition between dense and porous bands is abrupt, occurring over a few tens of micrometres (BSE images of samples B and C in Fig. 3). Microlites and microphenocrysts are aligned with the banding and thus with shear and extrusion direction (Fig. 3). The high shear region of the spine is further crosscut by multiple subparallel curvilinear extensional bands (i.e. weakly defined fractures) up to ∼ 1 m in length and trending ∼ 57° from the primary C–S fabrics in a Riedel-like fashion (Fig. 2c, d); some of these bands extend into the moderate shear zone but only faintly. These bands, spaced by 3–6 cm (∼ 4.5 cm in average), show opening of ca. 1–2 mm in places. (Note that the blue traces in Fig. 2 denote the general attitude, not the spacing, of the bands.) The Riedel fractures appear to be associated with a set of faint, conjugate fractures (R'), although their observation is not ubiquitous across the high shear zone.

The fault zone hosts up to ca. 0.2 m thick gouge material (Fig. 2c, d). The contact between the gouge and the high shear zone is generally sharp and often planar, although we observed small embayments, especially along C–S fabrics in the neighbouring high shear zone (Fig. 2d). (Note that the extent of the gouge is not exposed equally across the outcrop as material was likely lost during separation of this block from the main spine upon eruption, so the surface does not reflect the contact geometry. This material loss also led to obliteration of vestiges of a pseudotachylyte, suggested by local partial melting textures presented by Wallace et al., 2019.) The gouge is typified by well-consolidated, fine-grained cataclasite with some larger rounded clasts up to ∼ 15 mm in diameter (sample A; Fig. 2c inset). The gouge is matrix supported and displays a strong foliation parallel to the spine extrusion direction. Conjugate fractures form a dominant feature con-
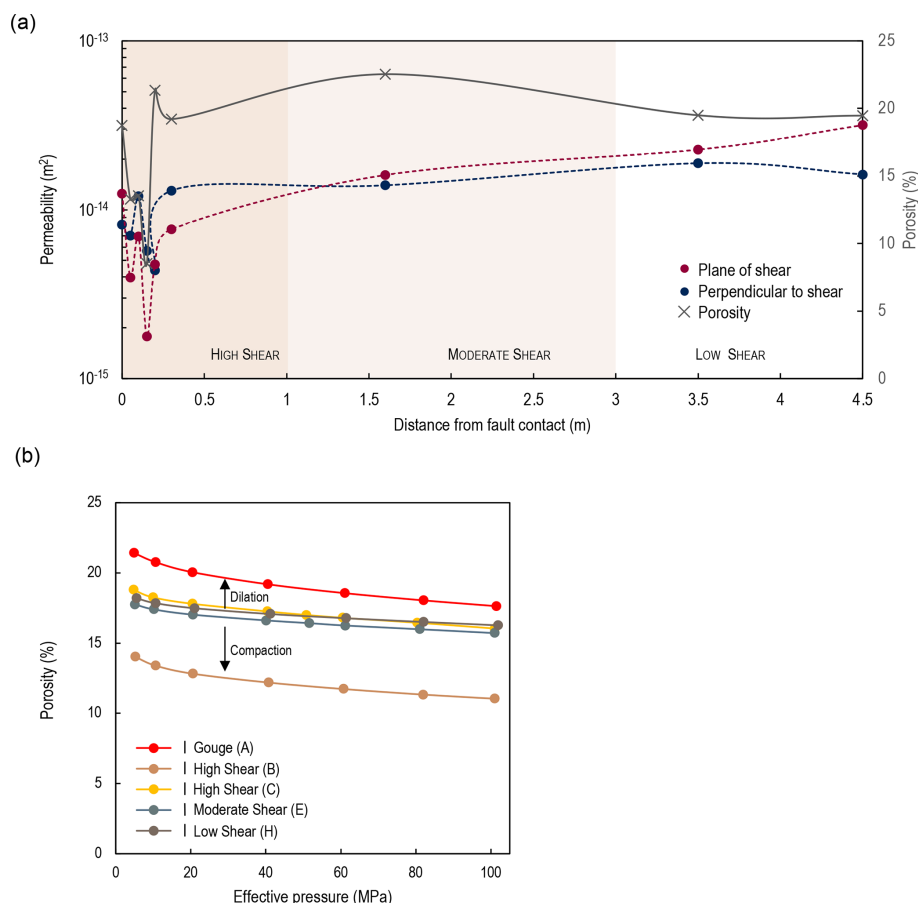
Figure 5. (a) Porosity and permeability (parallel and perpendicular to shear plane) profile across the shear zone (at $P_{eff} \simeq 5$ MPa), showing the compactant (ductile) nature of the high shear zone overprinted by localised, dilational (brittle) fractures. Measurements on the gouge sample are plotted at a distance of 0 m. **(b)** Porosity reduction as a function of effective pressure, derived from the volume of water expelled during loading in effective pressure of samples cored parallel to shear. Note that the initial porosity value (at $P_{eff} \simeq 5$ MPa) is that of the sample initial porosity (before loading); the exact quantity of water expelled between 0.1 and 5 MPa cannot be accurately determined due to the method used, and hence we simply show the porosity reduction from this point onward.

tributing to the porosity of the gouge. Microscopically, the rock is pervasively fragmented (sample A in Fig. 3); the few phenocrysts that remain relatively intact often display signs of deformation. The fragments in the gouge are generally densely compacted and the porosity is uniformly distributed, with little banding or preferred orientation of fragments at the microscopic scale, although connected pores occasionally exhibit a degree of alignment at small scale (Fig. 3) and at large scale as observed via X-ray tomography (Fig. 4a–b).

3.1.2 Connected porosity across the marginal shear zone

The porosity of the rocks, determined via pycnometry, indicates variations between 8 % and 27 % across the shear zone and in the fault gouge; Fig. 5a displays the average of multiple measurements from the different cores prepared from each sample. The measurements indicate that the high shear zone generally holds slightly lower porosities than sur-

rounding areas. Within the high shear zone (sample B) we measured significant variations in porosity ranging between 8 % and 15 % (at ambient conditions) due to flow bands (e.g. in sample B); yet, the coarseness of samples measured prevents accurate quantification of the highly spatially variable porosities observed in hand specimens.

When loading the samples (cored parallel to the spine extrusion direction) in the hydrostatic pressure vessel, we observed a nonlinear decrease in porosity of up to 4 % by increasing the effective pressure to 100 MPa (Fig. 5b). We observe a similar dependence of porosity on effective pressure for the coherent samples from the low, moderate, and (densest part of) high shear areas, with a slightly larger reduction in porosity with effective pressure in the initially most porous, high shear bands and the granular gouge sample (Fig. 5b).
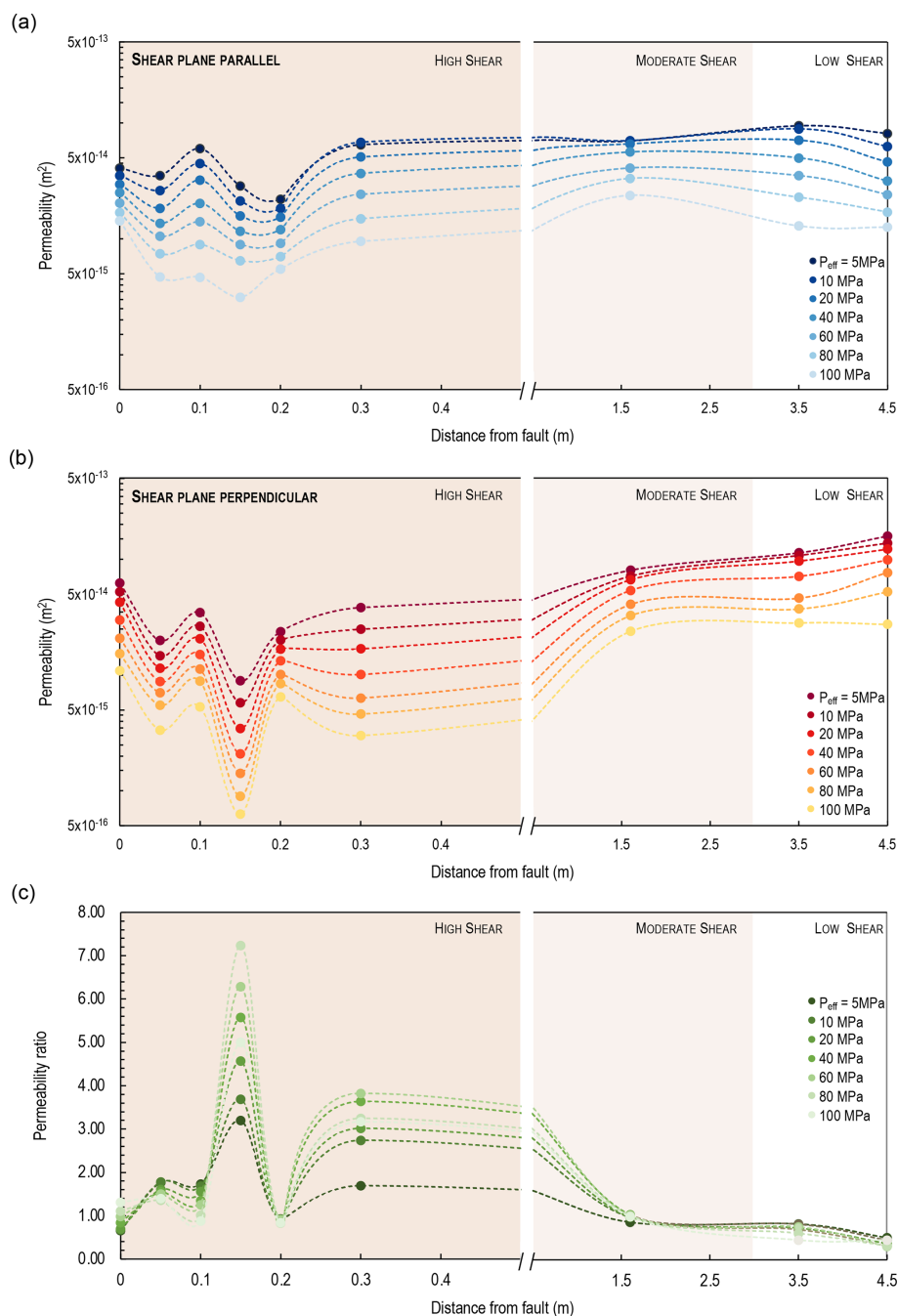
Figure 6. Permeability of the marginal shear zone as a function of effective pressure and direction to shear: measurements conducted **(a)** parallel and **(b)** perpendicular to the shear plane. The data show a reduction in permeability with effective pressure, yet the permeability profile across the shear zone remains, irrespective of the pressure conditions tested. The data show contrasting permeabilities as a function of direction, which create **(c)** permeability anisotropy, cast here as the ratio between the permeability parallel and perpendicular to the shear plane. The anisotropy is most pronounced in the high shear zone and generally increased as samples were loaded to higher effective pressure due to fracture closure. Note that the x axis was truncated and the scale was expanded for the near-fault high shear zone for which we conducted more measurements due to the structurally complex nature of this area of the spine. Measurements on the gouge sample are plotted at a distance of 0 m.

3.1.3 Permeability across the marginal shear zone

The permeability of the rocks collected across the spine segment reveals a ∼ 1 m wide region of low permeability in the high shear zone compared with the moderate shear zone, the low shear spine core, and the fault gouge (Figs. 5, 6). There appear to be abrupt variations in permeability (decrease and increase) in sheared rocks directly adjacent to the fault gouge due to the alternation between dense and porous shear bands.

There are considerable differences in the permeability parallel and perpendicular to the plane of shear (Fig. 3c, d) across the shear zone (Fig. 6a, b). In the high shear zone permeability was found to be higher in the plane of shear (i.e. parallel to the extrusion direction) than perpendicular to it, whereas in the moderate and low shear zones, as well as in the gouge, permeability was essentially isotropic. Anisotropy is cast here as a ratio between the permeability parallel and perpendicular to the shear plane (Fig. 6c). The anisotropy is most pronounced in the high shear zones, where, in one instance, the permeability ratio increases dramatically from 3 to over 7 times larger parallel than perpendicular to the shear plane with increasing confining pressure in a hydrostatic pressure vessel (Fig. 6c). In other samples, the anisotropy increase with pressure is less or even negligible, indicating the heterogenous nature of the high shear zone. This sensitivity to confinement is due to the presence of the distinct dense and porous bands in the sheared lava (Figs. 5b, 6); in the cores parallel to the shear plane, fluid can flow through porous bands from the top to bottom of the sample, whereas perpendicular to shear, fluids must pass through both and dense and porous bands to traverse the sample. Fluid flow in the denser areas will be dominated by channelling through narrow fractures (sub-horizontal in BSE images in samples B and C in Fig. 3), which are more susceptible to closure by increasing effective pressure than equant pores (e.g. Kendrick et al., 2021). Although this process occurs during confinement in both orientations, it only impacts permeability perpendicular to the shear direction and therefore contributes to enhanced anisotropy of permeability in banded shear fabrics under confinement (Kendrick et al., 2021).

3.2 Central shear zone

3.2.1 Structural observations

The second feature of interest is the cavity exposed in the central shear zone block (Figs. 1c and 2a). This section of the spine has been described in detail by Smith et al. (2001); here, we review key aspects observed in the field as no samples were collected to conserve the exposure of this world-class feature. We only examined the rocks forming this structure and performed non-destructive, in situ testing.

The central shear zone (CSZ) is located near the centre of the spine core (Fig. 1c). Its primary feature is the presence
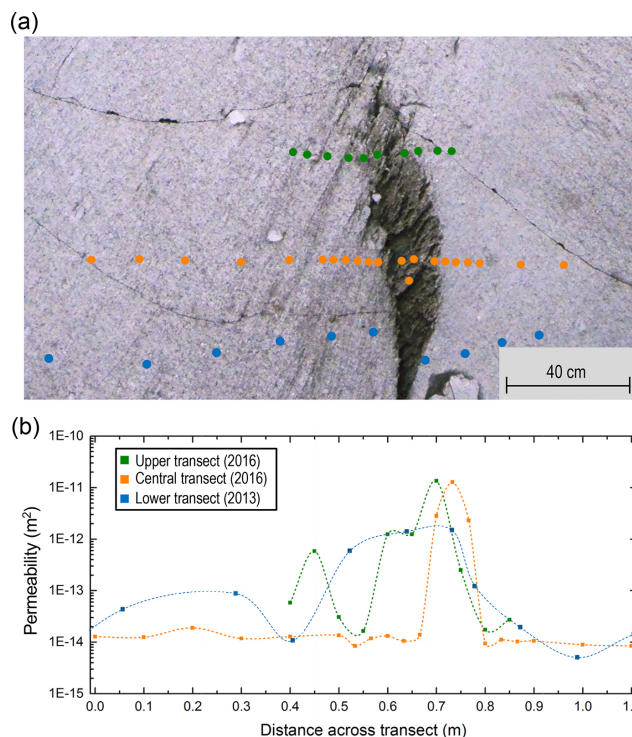

Figure 7. (a) Photograph showing measurement locations of the field-based permeability measurements for the upper (green), central (orange), and lower (blue) transects. **(b)** Permeability data for the upper (green), central (orange), and lower (blue) transects transects plotted against distance. The data show a drastic increase in permeability of ∼ 3 orders of magnitude.

of a porous cavity, which curves and pinches out (upward) from the end of a dominant, 9 cm wide fracture extending approximately 3 m in length (determined from the visible extent of the exposure). Unlike the aforementioned marginal shear zone, which displays an increased degree of shear towards the spine margin, the central shear zone exhibits an increase in shear towards the centre of the spine. From left to right (i.e. northward) in Fig. 7, we note an increase in aligned, bent, and broken phenocrysts as well as aligned shear bands (ostensibly parallel to the dominant fracture), fractures, and surface roughness, which terminates upon intersecting the end cavity; beyond this point, the rocks show no clear evidence of shear, including shear bands, elongate pores, or aligned crystals. This is evident in the field photograph (Fig. 7) as steeply inclined porous bands which end against the southern (i.e. left) side of the cavity; on the southern side the sheared lava exhibits a higher porosity than the surrounding undeformed rocks (although this could not be quantified in the field). Approximately 1 m above the pinched-out tip of the main cavity, we observe the presence of a secondary porous cavity (Fig. 1c inset) that is approximately 60 cm long and elongated parallel to the fracture that connects to the main cavity.

3.2.2 Permeability across the central shear zone

The permeability of the rocks in the central shear zone was measured along three transects in two field campaigns (in November 2013 and May 2016) to negate potential influence from variable degrees of water saturation of the rocks at different times of year. Our field measurements are consistent with one another. The permeability varies very little in the undeformed areas of the outcrop (i.e. on the right-hand side of the fracture in Fig. 7) for all transects, with an abrupt increase in permeability up to 3 orders of magnitude in the 9 cm wide central cavity and elevated permeability in the ~ 40 cm wide proximal sheared area to the left (south) of the fracture.

4 Interpretation

The contrasting permeability, porosity, and (micro)structural changes observed across the marginal and central shear zones reveal the impact of shear and distinct modes of magma deformation during shallow conduit ascent. Here we interpret each of these key features for the development of volcanism at lava domes.

4.1 Marginal shear zone

The marginal shear zone is characterised by a 3 m wide zone in which strain caused changes in the porous structure via crushing of the pore walls as well as distortion and failure of the crystalline phase; these promoted an increased reduction in pore volume and permeability towards the fault, especially in the high shear zone. Smith et al. (2001) invoked the effects of gravitational forces during post-emplacement flow of the lobes as a mechanism for the development of "ragged" pores and porous and/or dense flow banding in dome lavas at Unzen volcano. Yet, such diktytaxitic structures have been observed in small surficial dome blocks at Santiaguito volcano (Guatemala), which have not suffered from gravitational effects associated with flow along the flanks (Rhodes et al., 2018); they have also been observed at Merapi volcano, where they were attributed to late-stage gas filter pressing of a silica-rich melt phase (Kushnir et al., 2016). The commonality between these observations is that they occur in crystal-rich magmas, where crystals hamper the presence and distribution of exsolved fluids and interstitial melt, leading to ragged pore boundaries with protruding crystals. At Unzen, the character and distribution of the porous network rather evidence the importance of deformation, which was pervasive and commonly compactant in the marginal high shear zone. Experiments have shown that in the ductile field, material may deform by sustaining substantial compaction without the propensity for developing localised strain (Rutter, 1986) – a regime that generally results in a permeability reduction through shear (Ashwell et al., 2015; Kushnir et al., 2017b; Heap et al., 2015a, b). In this regime, magma deformation may result in crystal–plastic distortion and failure

(Kendrick et al., 2016), as witnessed at Unzen (Wallace et al., 2019). Thus, we interpret the bulk of the marginal shear zone as the result of ductile deformation, which resulted in distributed, pervasive shear over a width of 3 m. Within this part of the conduit, the high shear zone displayed the highest degree of shear-enhanced compaction.

However, ductility alone is insufficient to describe the marginal shear zone. For instance, the high shear area exhibits a foliation (S plane) and fractures (C plane) parallel to the shear plane, which is then crosscut (parallel but undulating) by a marginal fault hosting gouge formed by comminution and cataclasis containing conjugate fractures. The composite C–S fabric in the high shear zone is increasingly penetrative towards the fault core (at the gouge contact), and its parallel C and S planes indicate that the shear zone accommodated significant strain. This is supported by observation that curvilinear Riedel fractures have developed and overprinted the C–S fabric at an angle of 57° (see Ramsay, 1980). Such an angle is consistent with a lava body undergoing rupture following sustained ductile deformation (e.g. Lavallée et al., 2013); it is also consistent with the progressive thickening of a shear zone formed via simple shear with a small component (< 10 %) of pure shear (assuming pure and simple shear are planar; Fossen and Cavalcante, 2017); this minor pure shear component is further supported by the presence of weakly defined conjugate fractures crosscutting the Riedel fractures. Both the gouge and the fractures through the high shear zone were constrained to have locally higher permeability and porosity than the bulk of the shear zones: features characteristic of dilational deformation resulting from macroscopically brittle failure (Heap et al., 2015a, b; Laumonier et al., 2011). Riedel fractures generated in experimentally deformed magma have been described as important pathways to redistribute fluids across shear zones (Laumonier et al., 2011), and we anticipate the impact would be similar at Unzen; the Riedel fractures in the marginal shear zone only reached ~ 1 m in length, but the marginal shear zone in other blocks (Fig. 1d) contain oblique Riedel fractures that reach 2–5 m in length (Fig. 1d), which would have formed efficient fluid flow pathways. Thus, we interpret the marginal shear zones to reflect the evolution of magma shearing across the ductile to brittle transition during shallowing of the magma plug, which impacted fluid flow during the spine eruption.

4.2 Central shear zone

The central shear zone detailed in this study has a very different character. Macroscopic observations of numerous cracks suggest that it is dominantly dilational, as supported by the drastic increase in permeability towards the fault and cavity. Despite having opened by ~ 9 cm, the main fracture tip is blunted as it terminates in a curvilinear cavity and seemingly disappears before reappearing as a secondary cavity 1 m above (Fig. 1c inset). This is akin to areas of reduced

density that develop ahead of crack tips during material failure in the lab (e.g. Célarié et al., 2003) and indicates immature shear that was insufficient to enable the continuous propagation of a fault across the whole spine. This, in conjunction with the observation that shear becomes more pronounced towards the centre of the spine, suggests that the areas undergoing shear may have locally shifted towards the conduit core; yet, displacement was not extensive. The reason for this shift is difficult to assert, but we posit that the shallow calving of blocks from the spine front, progressive inward cooling, and/or the higher porosity of the magmas in the conduit core (compared to a denser, compacted, and strained conduit margin) may have shifted the locus of deformation towards the conduit core at the end of the eruption.

The shear zones studied here indicate that the dominant deformation regime of magma may evolve spatially and temporally during ascent in volcanic conduits, which would modify the magma's permeability and its ability to localise and channel outgassing during the effusion of lava domes.

5 Discussion

5.1 Permeability in volcanic environments

The power of volcanic eruption models relies on an understanding of the coupling between magma and volatiles in volcanic conduits (Sparks, 1997), yet a description of dynamic permeability of deforming magma eludes us. The studies of eruptive products have provided first-order constraints on the relationship between permeability and porosity (Fig. 8; Klug and Cashman, 1996; Mueller et al., 2005; Farquharson et al., 2015) for various types of volcanic rocks (e.g. explosive clasts vs. effusive lavas), including the presence of heterogeneous structures (Farquharson et al., 2016c; Kolzenburg et al., 2012; Lamur et al., 2017; Kendrick et al., 2021), and these constraints have been invoked in diverse models to assess how magma permeability may evolve leading to eruption (Burgisser et al., 2019; Edmonds et al., 2003). However, the deformability of magma imposes constant changes to the porous permeable network, and to date, only a few studies have measured or assessed the transience of permeability and porosity during magma deformation (Okumura et al., 2010, 2012; Kendrick et al., 2013; Ashwell et al., 2015; Kennedy et al., 2016), especially in operando (Wadsworth et al., 2017, 2021; Kushnir et al., 2017a; Heap et al., 2017b). Considering the range of pressure conditions (e.g. pore pressure gradient, local deviatoric stress) and magma properties, none of these studies have yet succeeded in fully reconstructing the evolution of porosity and permeability of magma shearing during ascent in volcanic conduits.

The rocks sampled across the shear zone and in the fault gouge at Mount Unzen vary in porosity between 8 % and 27 %; this range is slightly narrower than the porosity range (4 %–48 %) covered by blocks shed by pyroclastic density currents originating from the domes during the 5-year eruption (see Fig. 8; Kueppers et al., 2005; Coats et al., 2018; Kendrick et al., 2021; Scheu et al., 2007; Mueller et al., 2005). The narrower range exhibited by the spine shear zones may reflect the occurrence of fewer porosity-modifying mechanisms (e.g. post-fragmentation vesiculation) in the highly viscous spine lava compared to those which occurred throughout the entire course of the eruption; these are represented by the blocks at the foot of the volcano. We see the largest contrast when we compare the permeability range of the lavas which erupted through the spine at the end of the eruption ($\sim 10^{-15}$ to $\sim 10^{-14}$ m^2, at the lowest effective pressure) with that obtained from rocks recovered by drilling through the eruptive conduit at a depth of ~ 1.5 km ($\sim 10^{-17}$ to $\sim 10^{-19}$ m^2) in the framework of the Unzen Scientific Drilling Project, drill hole 4 (USDP-4) (Watanabe et al., 2008). The latter rocks, originating from magma stalling at depth, reflect greater time under compactant conditions, porosity infill, and reduction from secondary mineral precipitation (Yilmaz et al., 2021). The large difference in permeability between the two datasets alludes to the highly variable spatial and temporal variation of magma permeability within even a single volcanic system.

Previous investigations of permeability in shallow volcanic conduits have highlighted the existence of dilational shear zones, whereby the conduit margin is bound by a permeable "damage halo"; this has been proposed through both field (Saubin et al., 2019; Pallister et al., 2013a; Gaunt et al., 2014; Wallace et al., 2019; Ryan et al., 2020; Sparks et al., 2000; Watts et al., 2002; Holland et al., 2011) and laboratory (Lavallée et al., 2013; Laumonier et al., 2011) studies. These constraints indicate a dilation zone, with permeability higher by up to 1.5 orders of magnitude and variable degrees of anisotropic shear fabrics, causing preferential channelling of fluids in the direction of extrusion (Wright et al., 2006; Gaunt et al., 2014; Wallace et al., 2019; Ryan et al., 2020). Pore space connectivity is enhanced by fracturing (Lamur et al., 2017; Tiab and Donaldson, 2016), which would contribute to the development of anisotropy and would preferentially channel fluids along the conduit margin, promoting concentric or ring-like gas emissions, for instance as exemplified at Santiaguito, Guatemala (Lavallée et al., 2013; Holland et al., 2011). Connectivity may, however, be lost at the expense of fracture healing (Lamur et al., 2019) or sintering (Ryan et al., 2020; Wadsworth et al., 2016). Here, at the conduit centre at Unzen, we observed a localised dilational shear zone up to 3 orders of magnitude more permeable than the surrounding magma; thus, the scale of dilation exceeds that observed in marginal shear zones at Mt. St. Helens (Gaunt et al., 2014) and at Chaos Crags (Ryan et al., 2020). This zone spans a relatively narrow section of the conduit and appears to be a late, immature feature that is possibly related to shear during the final stages of ascent of the magma plug and/or structural readjustment during failure and calving of portions of the spine to the ENE. Instead, the primary (and
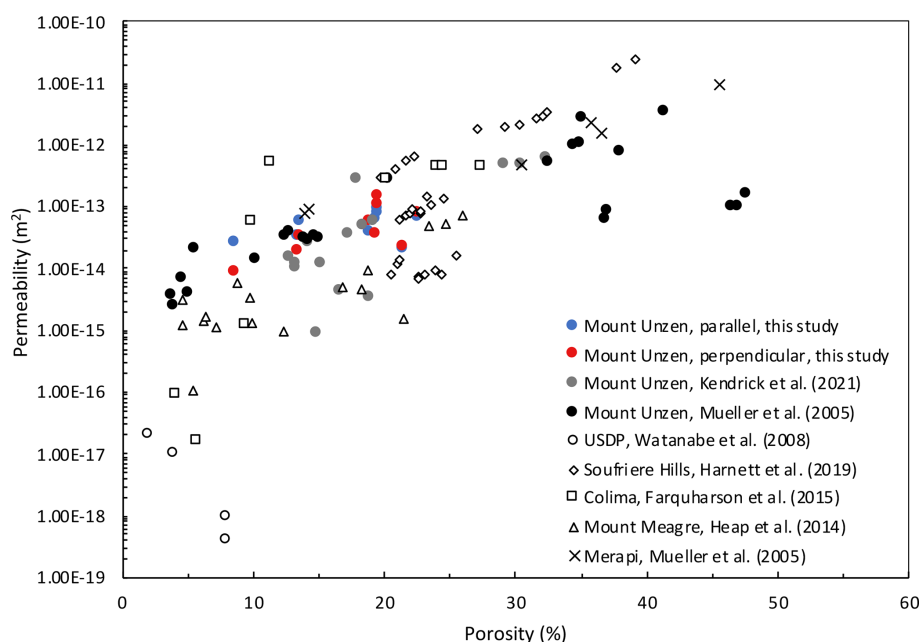
Figure 8. Permeability–porosity relationship for Unzen dome lavas and other volcanic products. Blue and red circles represent data from this study, made parallel and perpendicular to the plane of shear, respectively. Grey circles show porosity data for Unzen from Mueller et al. (2005) and Kendrick et al. (2021), and open circles show permeability measurement on USDP drill cores from Watanabe et al. (2008). Other symbols indicate porosity–permeability measurements for volcanic materials from Soufriere Hills volcano (Harnett et al., 2019), Volcán de Colima (Farquharson et al., 2015), Mount Meagre (Heap et al., 2014), and Merapi volcano (Mueller et al., 2005).

volumetrically most significant) marginal shear zone studied at Unzen is mostly compactional and exhibits a lower permeability than the surrounding magma, particularly in the plane perpendicular to shear direction. Compaction may have been favoured in the marginal shear zone at Unzen compared to dilation at Mt. St. Helens and Chaos Crags due to the relatively higher porosity of the ascending magma (20 % at Unzen vs. 10 % and 12 %–15 % at Mt. St. Helens and Chaos Crags, respectively; Gaunt et al., 2014; Ryan et al., 2020); it may also reflect lower viscosities and/or deformation at greater effective mean stress in the system or at relatively lower strain rates (Fig. 9). Indeed, the marginal shear zone is overprinted by faulting, which suggests that compaction took place at greater depth and/or during inter-seismic periods of slower ascent. Seismic analysis indicated that seismogenic faulting was episodic and shallow, likely originating in the upper 500 m of the conduit (Umakoshi et al., 2008; Lamb et al., 2015); so, whilst below this depth shear may have prompted compaction, above this depth pulsatory magma shearing may have resulted in switches between compactional and dilatant shear, causing locally higher-permeability fractures through the sheared magma and a permeable marginal fault gouge by cataclasis (Fig. 9). Such intermittent seismic stressing may also serve to weaken surrounding country rocks and modify permeable pathways (Schaefer et al., 2020).

5.2 Ductile–brittle transition in ascending magma

The presence and overprinting of compactional and dilational shearing modes in close proximity within a given magmatic extrusion demand appraisal. The ductile–brittle transition of materials has long been studied and is generally better understood for rocks than magmas as more low-temperature tests have been carried out (Paterson and Wong, 2005; Rutter, 1986; Heap et al., 2015a). Reconstruction of yield caps (or curves), based on the shear stress required for rupture or flow of materials at different effective mean stress, has shown that porous rocks undergo a transition from macroscopically brittle to ductile deformation mode with increasing effective pressure (Fig. 9b); this transition sets in at lower effective pressure (i.e. either at shallower depths or with higher pore pressures) if the material is more porous (Heap et al., 2015a). However, magma is viscoelastic; thus, depending on the timescale of observations, magma may behave as a solid: in essence, as a rock. Magmas abide by the glass transition so that at long observation timescales or under slow deformation, they flow; but at short timescales or if strain rate is high, they may rupture (Dingwell, 1996). The strain rate to meet this transition decreases if melt viscosity increases due to cooling, crystallisation, degassing, and/or vesiculation (Wadsworth et al., 2018; Dingwell and Webb, 1989, 1990; Cordonnier et al., 2012, 2009; Coats et al., 2018; Lavallée et al., 2013, 2008). The glass transition of silicate melts, which controls the deformation mechanisms of magmas (viscous
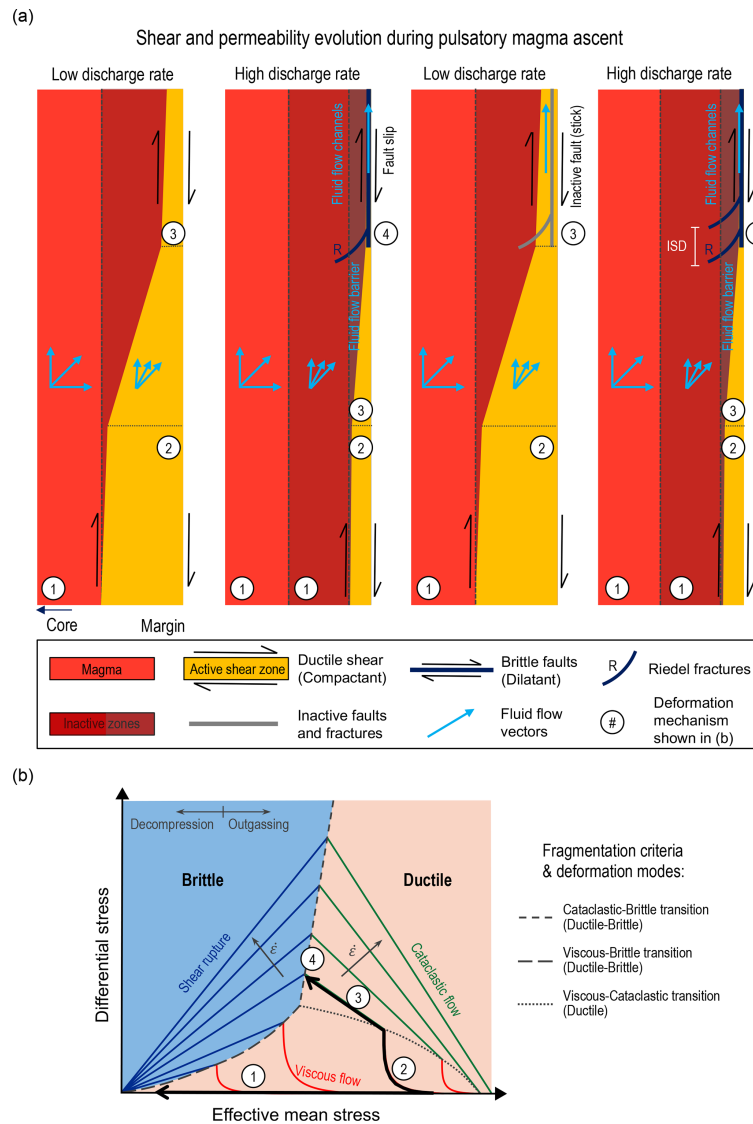
Figure 9. (a) Conceptual model showing rheological shifts and evolution of permeability (seen as fluid flow vectors) during pulsatory magma ascent and stick-slip faulting. The sketches illustrate the evolution of the extent of active shear zones (in orange), inactive areas (dark reds), active faults (blue), and inactive faults (grey) during magma discharge fluctuations through time. The dominant rheology in each area is numbered (1–4) and is linked to the deformation mechanism map for magma (shown in **b**). The sketches **(a)** show that shear narrows toward the eruption point as magmas are subjected to lower effective pressure (as shown in **b**). Compaction of the outer margin of the shear zones (dark red–brown) would generate a zone of lower permeability (which may act as a local fluid flow barrier). As discharge rates increase, the width of the shear zone also narrows and promotes a switch to brittle failure at shallow depth (~ 500 m), causing the propagation of a primary fault plane and an adjacent Riedel fracture (which channels fluid flow; blue arrow). Upon discharge rate reduction, the shear zone would widen again and the fault would become inactive (stick phase), shifting the Riedel fracture to shallower depth. Upon renewed discharge rate increase, shear would narrow again, and faulting would generate another Riedel fracture. Thus, the distance between Riedel fractures may be used to resolve the magma ascent associated with inter-seismic deformation (ISD). **(b)** Sketch of a deformation mechanism map for magma (adapted from Lavallée and Kendrick, 2020). At low differential stresses magma flows viscously, but at higher differential stresses, magma may undergo the glass transition and the deformation mode may switch to brittle rupture (dilatant shear) or ductile cataclastic flow (compactant shear), depending on the effective mean stress. These deformation modes form yield caps, displayed by the blue and green lines representing brittle rupture and ductile cataclastic flow, respectively. Each line refers to a given strain rate condition, and the sketch shows an increase in strength as a function of strain rate ($\dot{\varepsilon}$); in the brittle field, the strain rate may increase with differential stress and/or by lowering the effective mean stress, whilst in the ductile field, the strain rate may increase with differential stress as well as effective mean stress. The inset double-headed arrow indicates magmatic scenarios which may influence the effective mean stress: for instance, decompression or pore pressurisation may reduce the effective mean stress, whilst outgassing may increase it. The numbers refer to scenarios as displayed for different parts of the magmatic column in **(a)**.

or brittle), thus impacts their deformation mode, brittle or ductile (be it viscous flow or cataclastic flow); applicability of the concept of yield caps to volcanic rocks and magmas, as shown in Fig. 9b, has been reviewed by Lavallée and Kendrick (2020). In a scenario in which magma ascends, deforms, and outgasses during an eruption, such as during spine extrusion at Unzen, magma may undergo a transition from a macroscopically ductile to brittle deformation mode due to a reduction in effective pressure (from ascent or due to pore pressure increase; Heap et al., 2017b), densification (Heap et al., 2015a; Coats et al., 2018), viscosity increase (see Dingwell and Webb, 1990), or if the strain rate locally increases (Coats et al., 2018; Lavallée et al., 2013, 2008).

Nakada and Motomura (1999) proposed that faulting of this spine formed due to a lower effusion rate that resulted in more complete degassing and crystallisation that increased the magma viscosity. We advance the idea that fluctuations in pore pressure (Farquharson et al., 2016a) and local strain rates (Coats et al., 2018; Lavallée et al., 2013; Wadsworth et al., 2019) may be especially important in triggering embrittlement of otherwise ductile magma. In the ductile regime, strain is accommodated over a prolonged duration without necessarily leading to any substantial stress drop (Coats et al., 2018). Thus, under such conditions, we do not expect to detect any, or much, seismicity that would characterise magma rupture near the conduit margin (e.g. Neuberg et al., 2006; Thomas and Neuberg, 2012; Kendrick et al., 2014b). As a result, we anticipate that magma shearing below the point of rupture (ca. 0.5 km at Unzen; Umakoshi et al., 2008) would have compacted and partially shut the permeability of the conduit margin, with the shear zone creating an impermeable barrier preventing gas from escaping to the surrounding country rock and promoting outgassing through the more permeable conduit core, at least up to the point of rupture (see Collinson and Neuberg, 2012). Upon further ascent, changes in the stress fields and physical properties of the magmas during pulsatory ascent would have favoured transition to a macroscopically brittle response to shear (Lavallée and Kendrick, 2020), triggering seismic rupture (Umakoshi et al., 2008; Lamb et al., 2015) and initiation of predominantly fault-controlled, stick-slip dynamics in the final stint of magma ascent and spine extrusion (Hornby et al., 2015). In brief periods of high discharge rate, shear may have localised along the primary seismogenic fault, simultaneously creating a Riedel fracture, but in periods with lower discharge rates, shear would have been distributed over a wide area and the fault would become inactive (stick phase), shifting the Riedel fractures to shallower depth; upon renewed discharge rate increase, shear would narrow again, faulting would generate another Riedel fracture, and so on (Fig. 9a). Indeed, using seismic events as a proxy for the ductile–brittle transition it was possible to identify its migration through time as the inclined spine loaded and compacted its lower shear zone as it grew, dilating the upper fault zone (Lamb et al., 2015). This is further indicated by the localisation of fumaroles along the upper spine margin (also observed during our latest field campaign in 2016), showing that the fault zone around the inclined spine controlled fluid circulation in the upper conduit (Lamb et al., 2015; Yamasato, 1998). Finally, a late lateral shift in dilational shearing, from the conduit margin to the conduit core, suggests that the location of shear may migrate during magma ascent in conduits as a result of changes in local stresses (e.g. upon extrusion and/or block calving), likely resulting from a combination of pore pressure fluctuations, strain rate reduction, and progressive inward cooling, which would have favoured deformation in the core of the spine. Thus, the rheology of magma and the dominant shearing mode may evolve during ascent, which in turn dynamically modifies the permeability distribution across the conduit through time (Fig. 9a).

5.3 Rheological assessment of magma switching from ductile to brittle deformation

The above rheological description is primarily based on the unavoidable decompression of erupting magma (which degasses, crystallises, and viscously stiffens), yet previous observations at Unzen suggest that the conditions for magmatic flow may have fluctuated (Umakoshi et al., 2008; Lamb et al., 2015), thus contributing to rheological shifts. Here, we invoke findings from the literature to assess the conditions leading to rupture. The discharge rates associated with spine extrusion in 1994–1995 varied, although Yamashina et al. (1999) constrained a relatively constant spine protrusion rate of $0.8 \, \text{m} \, \text{d}^{-1}$ over a week-long period in early November 1994. Scrutinising within this period, however, seismicity indicated a pulsatory magma ascent in the conduit at shorter timescales (Umakoshi et al., 2008; Lamb et al., 2015). In particular, waveform correlation of the seismic record performed by Lamb et al. (2015) revealed rhythmic seismicity punctuated by two primary clusters that were attributed to recurring rupture associated with stick-slip cycles. They identified 668 repetitive events over the course of the 36 d examined: 487 from cluster 1 and 181 from cluster 2. Progressive shallowing of the cluster 1 source location was argued to result from progressive compaction of the lower shear zone (underneath the inclined magma column) as the eruption slowly waned; in contrast, cluster 2, which was accompanied by low-frequency coda associated with fluid resonance, showed deepening of the source location due to dilation on the overside of the inclined conduit. Considering the events in cluster 1, we define the recurrence rate of fault slip at 13.5 events per day, so each "stick" interval for viscous flow would have lasted on average 106 min. Hornby et al. (2015) statistically analysed the slip duration of seismic events in clusters 1 and 2, defining a mode and mean of 0.1 s. In order to pursue a quantitative analysis of stick-slip behaviour, we must first turn our attention to our knowledge of Unzen magma flow and failure conditions.

Coats et al. (2018) studied the rheology of Unzen's porous lavas to define a failure criterion. Considering the estimated eruptive temperature of ca. 870–900 °C (Holtz et al., 2005; Venezky and Rutherford, 1999) and measured glass transition temperature (at 10 °C min^{-1}) of 790 °C (Wallace et al., 2019), Coats et al. (2018) empirically determined that Unzen magma would break if experiencing strain rates exceeding $\sim 10^{-3}$ s^{-1}; otherwise, magma would undergo ductile flow. But these determinations were done at atmospheric pressure, so the melt was considered dry. Kusakabe et al. (1999) determined the concentration of magmatic water dissolved in the groundmass glass of eruptive products at 0.1 wt %–0.5 wt %; however, the concentration of dissolved water at the point of rupture, at 500 m depth or ~ 10 MPa pressure considering a nominal rock density of ~ 2000 kg m^{-3} (Scheu et al., 2006), would have been ~ 1 wt % (Liu et al., 2005). Such a higher concentration would lower the viscosity of the interstitial melt by 1 order of magnitude; as the strain rate limit shares an inverse relationship with viscosity (e.g. Dingwell and Webb, 1989), we advance the idea that the presence of dissolved water in the melt would have shifted the strain rate limit by approximately 1 order of magnitude. If we omit any upscaling of the above failure conditions for simplification and assume that deformation was localised in the ~ 1 m wide high shear area of the spine, rupture would have occurred when the ascent rate exceeded 1 mm s^{-1}. As such high-deformation-rate episodes are inferred to have triggered fault slip events lasting on average 0.1 s (Hornby et al., 2015), each slip event may have resulted in a mere 0.1 mm of displacement. With 13.5 events per day, this would culminate in 1.35 mm of magma ascent ascribed to faulting activity, signifying that deformation associated with the ~ 0.8 m daily ascent was predominantly ductile and aseismic.

We can then turn our attention to geometrical constraints from our structural analysis to frame magma ascent conditions that satisfy the above failure criterion. The Riedel fractures that are observed at regular intervals of ~ 4.5 cm in the high shear zones have been shown to be important stress and strain rate distribution markers in multiphase materials containing a weak phase, such as melt and bubbles (Finch et al., 2020), and can thus be used to constrain rates. Considering the ephemeral nature of Riedel fracture development (Finch et al., 2020), here we assume that their formation may be encouraged during brief periods of high strain rate, and they thus portray the clockwork ticking of seismogenic slip events during magma ascent. Bearing in mind an average spacing of 4.5 cm and an angle of 57° with respect to the main C–S fabric, we estimate the offset of the loci of rupture events at 5.4 cm. Recalling the 0.1 mm of displacement ascribed to faulting events (detailed in the previous paragraph), this suggests that ductile deformation was responsible for 5.3 cm of magma ascent during inter-seismic periods (i.e. inter-seismicity deformation, ISD; Fig. 9a). Again, considering shear over a 1 m area and inter-seismic periods of 106 min, we estimate that ductile deformation would have

proceeded at an average rate of 8×10^{-6} s^{-1}, which is a value well within the ductile regime as experimentally constrained by Coats et al. (2018). The above rates (of magma flow in the ductile regime and of faulting) may be conservative estimates, especially if we consider the rheological consequences of dissolved water at depth. Even if the threshold strain rate for seismogenic faulting were an order of magnitude higher at 10^{-2} s^{-1}, this would only require 13.5 mm of magma ascent in each brittle faulting event, and inter-seismic periods of ductile deformation at a rate of $\sim 8 \times 10^{-5}$ s^{-1} would have dominated spine extrusion.

In concert the physical and structural descriptions bolstered by the rheological analysis argue for changes in magma rheology during decompression and pulsatory ascent. We propose that throughout its journey to the Earth's surface, magma may undergo several cycles of expansion (from vesiculation and dilation) and collapse (from outgassing and compaction) due to variable permeability and pore pressure, which may promote switches in shearing regimes that trigger further changes in the permeability structure of shallow conduits. For instance, the vesicles of low-permeability magma may accumulate fluid, thus reducing the effective pressure and promoting brittle, dilatant rupture; rupture would in turn allow magma outgassing and a reduction in effective pressure, promoting compaction and lowering of permeability, and the cycle may recur. The picture portrayed here highlights the need to understand the coupling between magma, fluid flow dynamics, and, importantly, pressure fluctuations (Michaut et al., 2013) in volcanic conduits with increased spatial and temporal complexities in order to resolve the transient state of magma and reconcile gas emission data and volcanic eruption style (Edmonds and Herd, 2007).

6 Conclusions

The present detailed study of the Mount Unzen spine reveals the competing occurrence of compactional and dilational shear regimes during magma ascent in volcanic conduits. At depth, in areas subjected to high effective pressure, shearing may induce pore compaction, thereby lowering the permeability of the system and inhibiting lateral outgassing to the country rock. At shallower depth, where the effective pressure may be low, shearing may favour localised dilation that enhances permeability. Both shear regimes result in the development of permeability anisotropy, with permeability generally being highest parallel or sub-parallel to the direction of extrusion and lowest perpendicular to the shear plane. The observation of shearing mode overprints suggests that fluctuations in effective pressure and strain rates, during stick-slip cycles, may result in magma switching between compactant and dilational shearing regimes, thus dynamically reshaping fluid circulation at a range of scales and in turn controlling outgassing efficiency during magma ascent and eruption.

References

Acocella, V.: Hazard mitigation of unstable volcanic edifices, EOS, 91, 357–358, https://doi.org/10.1029/2010EO400002, 2010.

Alidibirov, M. and Dingwell, D. B.: Magma fragmentation by rapid decompression, Nature, 380, 146–148, 1996.

Ashwell, P. A., Kendrick, J. E., Lavallée, Y., Kennedy, B. M., Hess, K. U., von Aulock, F. W., Wadsworth, F. B., Vasseur, J., and Dingwell, D. B.: Permeability of compacting porous lavas, J. Geophys. Res.-Sol. Ea., 120, 1605–1622, https://doi.org/10.1002/2014jb011519, 2015.

Baker, D. R., Brun, F., O'Shaughnessy, C., Mancini, L., Fife, J. L., and Rivers, M.: A four-dimensional X-ray tomographic microscopy study of bubble growth in basaltic foam, Nat. Commun., 3, 1135, https://doi.org/10.1038/ncomms2134, 2012.

Ball, J. L., Stauffer, P. H., Calder, E. S., and Valentine, G. A.: The hydrothermal alteration of cooling lava domes, B. Volcanol., 77, 102, https://doi.org/10.1007/s00445-015-0986-z, 2015.

Blower, J. D.: Factors controlling permeability-porosity relationships in magma, B. Volcanol., 63, 497–504, 2001.

Blundy, J., Cashman, K., and Humphreys, M.: Magma heating by decompression-driven crystallization beneath andesite volcanoes, Nature, 443, 76–80, https://doi.org/10.1038/nature05100, 2006.

Brace, W. F., Walsh, J. B., and Frangos, W. T.: Permeability of granite under high pressure, J. Geophys. Res., 73, 2225–2236, https://doi.org/10.1029/JB073i006p02225, 1968.

Browning, J., Tuffen, H., James, M. R., Owen, J., Castro, J. M., Halliwell, S., and Wehbe, K.: Post-fragmentation vesiculation timescales in hydrous rhyolitic bombs from Chaitén volcano, J. S. Am. Earth Sci., 104, 102807, https://doi.org/10.1016/j.jsames.2020.102807, 2020.

Burgisser, A., Chevalier, L., Gardner, J. E., and Castro, J. M.: The percolation threshold and permeability evolution of ascending magmas, Earth Planet. Sci. Lett., 470, 37–47, https://doi.org/10.1016/j.epsl.2017.04.023, 2017.

Burgisser, A., Bechon, T., Chevalier, L., Collombet, M., Arbaret, L., and Forien, M.: Conduit processes during the February 11, 2010 Vulcanian eruption of Soufriere Hills, Montserrat, J. Volcanol. Geoth. Res., 373, 23–35, https://doi.org/10.1016/j.jvolgeores.2019.01.020, 2019.

Calder, E. S., Lavallée, Y., Kendrick, J. E., and Bernstein, M.: Chapter 18 – Lava Dome Eruptions. The Encyclopedia of Volcanoes, 2nd Edn., edited by: Sigurdsson, H., Amsterdam, Academic Press, 343–362, 2015.

Caricchi, L., Burlini, L., Ulmer, P., Gerya, T., Vassalli, M., and Papale, P.: Non-Newtonian rheology of crystal-bearing magmas and implications for magma ascent dynamics, Earth Planet. Sc. Lett., 264, 402–419, 2007.

Cashman, K. and Blundy, J.: Degassing and Crystallization of ascending andesite and dacite, Philos. T. R. Soc. Lond., 358, 1487–1513, 2000.

Castro, J. M. and Gardner, J. E.: Did magma ascent rate control the explosive-effusive transition at the Inyo volcanic chain, California?, Geology, 36, 279–282, https://doi.org/10.1130/g24453a.1, 2008.

Castro, J. M., Cordonnier, B., Tuffen, H., Tobin, M. J., Puskar, L., Martin, M. C., and Bechtel, H. A.: The role of melt-fracture degassing in defusing explosive rhyolite eruptions

at volcan Chaiten, Earth Planet. Sc. Lett., 333, 63–69, https://doi.org/10.1016/j.epsl.2012.04.024, 2012.

Célarié, F., Prades, S., Bonamy, D., Ferrero, L., Bouchaud, E., Guillot, C., and Marliere, C.: Glass breaks like metal, but at the nanometer scale, Phys. Rev. Lett., 90, 075504, https://doi.org/10.1103/PhysRevLett.90.075504, 2003.

Chouet, B. A.: Long-period volcano seismicity: Its source and use in eruption forecasting, Nature, 380, 309–316, 1996.

Coats, R., Kendrick, J. E., Wallace, P. A., Miwa, T., Hornby, A. J., Ashworth, J. D., Matsushima, T., and Lavallée, Y.: Failure criteria for porous dome rocks and lavas: a study of Mt. Unzen, Japan, Solid Earth, 9, 1299–1328, https://doi.org/10.5194/se-9-1299-2018, 2018.

Collinson, A. S. D. and Neuberg, J. W.: Gas storage, transport and pressure changes in an evolving permeable volcanic edifice, J. Volcanol. Geoth. Res., 243, 1–13, https://doi.org/10.1016/j.jvolgeores.2012.06.027, 2012.

Colombier, M., Wadsworth, F. B., Gurioli, L., Scheu, B., Kueppers, U., Di Muro, A., and Dingwell, D. B.: The evolution of pore connectivity in volcanic rocks, Earth Planet. Sc. Lett., 462, 99–109, https://doi.org/10.1016/j.epsl.2017.01.011, 2017.

Cordonnier, B., Hess, K. U., Lavallée, Y., and Dingwell, D. B.: Rheological properties of dome lavas: Case study of Unzen volcano, Earth Planet. Sc. Lett., 279, 263–272, https://doi.org/10.1016/j.epsl.2009.01.014, 2009.

Cordonnier, B., Caricchi, L., Pistone, M., Castro, J., Hess, K. U., Gottschaller, S., Manga, M., Dingwell, D. B., and Burlini, L.: The viscous-brittle transition of crystal-bearing silicic melt: Direct observation of magma rupture and healing, Geology, 40, 611–614, https://doi.org/10.1130/g3914.1, 2012.

Degruyter, W., Bachmann, O., Burgisser, A., and Manga, M.: The effects of outgassing on the transition between effusive and explosive silicic eruptions, Earth Planet. Sc. Lett., 349, 161–170, https://doi.org/10.1016/j.epsl.2012.06.056, 2012.

Dingwell, D. B.: Volcanic dilemma: flow or blow?, Science, 273, 1054–1055, 1996.

Dingwell, D. B. and Webb, S. L.: Structural relaxation in silicate melts and non-Newtonian melt rheology in geologic processes, Phys. Chem. Miner., 16, 508–516, 1989.

Dingwell, D. B. and Webb, S. L.: Relaxation in silicate melts, Eur. J. Mineral., 2, 427–449, 1990.

Dingwell, D. B., Lavallée, Y., Hess, K.-U., Flaws, A., Marti, J., Nichols, A. R. L., Gilg, H. A., and Schillinger, B.: Eruptive shearing of tube pumice: pure and simple, Solid Earth, 7, 1383–1393, https://doi.org/10.5194/se-7-1383-2016, 2016.

Edmonds, M. and Herd, R. A.: A volcanic degassing event at the explosive-effusive transition, Geophys. Res. Lett., 34, L21310, https://doi.org/10.1029/2007gl031379, 2007.

Edmonds, M., Oppenheimer, C., Pyle, D. M., Herd, R. A., and Thompson, G.: SO_2 emissions from Soufriere Hills Volcano and their relationship to conduit permeability, hydrothermal interaction and degassing regime, J. Volcanol. Geoth. Res., 124, 23–43, 10.1016/s0377-0273(03)00041-6, 2003.

Eggertsson, G. H., Lavallée, Y., Kendrick, J. E., and Markússon, S. H.: Improving fluid flow in geothermal reservoirs by thermal and mechanical stimulation: The case of Krafla volcano, Iceland, J. Volcanol. Geoth. Res., 391, 106351, https://doi.org/10.1016/j.jvolgeores.2018.04.008, 2020.

Eichelberger, J. C., Carrigan, C. R., Westrich, H. R., and Price, R. H.: Non-explosive silicic volcanism, Nature, 323, 598–602, https://doi.org/10.1038/323598a0, 1986.

Farquharson, J., Heap, M. J., Varley, N. R., Baud, P., and Reuschle, T.: Permeability and porosity relationships of edifice-forming andesites: A combined field and laboratory study, J. Volcanol. Geoth. Res., 297, 52–68, https://doi.org/10.1016/j.jvolgeores.2015.03.016, 2015.

Farquharson, J., Heap, M. J., Baud, P., Reuschle, T., and Varley, N. R.: Pore pressure embrittlement in a volcanic edifice, B. Volcanol., 78, 6, https://doi.org/10.1007/s00445-015-0997-9, 2016a.

Farquharson, J. I., Heap, M. J., and Baud, P.: Strain-induced permeability increase in volcanic rock, Geophys. Res. Lett., 43, 11603–11610, https://doi.org/10.1002/2016gl071540, 2016b.

Farquharson, J. I., Heap, M. J., Lavallée, Y., Varley, N. R., and Baud, P.: Evidence for the development of permeability anisotropy in lava domes and volcanic conduits, J. Volcanol. Geoth. Res., 323, 163–185, https://doi.org/10.1016/j.jvolgeores.2016.05.007, 2016c.

Farquharson, J. I., Wadsworth, F. B., Heap, M. J., and Baud, P.: Time-dependent permeability evolution in compacting volcanic fracture systems and implications for gas overpressure, J. Volcanol. Geoth. Res., 339, 81–97, https://doi.org/10.1016/j.jvolgeores.2017.04.025, 2017.

Finch, M. A., Bons, P. D., Steinbach, F., Griera, A., Llorens, M.-G., Gomez-Rivas, E., Ran, H., and de Riese, T.: The ephemeral development of C' shear bands: A numerical modelling approach, J. Struct. Geol., 139, 104091, https://doi.org/10.1016/j.jsg.2020.104091, 2020.

Fossen, H. and Cavalcante, G. C. G.: Shear zones – A review, Earth-Sci. Rev., 171, 434–455, https://doi.org/10.1016/j.earscirev.2017.05.002, 2017.

Gaunt, H. E., Sammonds, P. R., Meredith, P. G., Smith, R., and Pallister, J. S.: Pathways for degassing during the lava dome eruption of Mount St. Helens 2004–2008, Geology, 42, 947–950, https://doi.org/10.1130/g35940.1, 2014.

Gaunt, H. E., Sammonds, P. R., Meredith, P. G., and Chadderton, A.: Effect of temperature on the permeability of lava dome rocks from the 2004–2008 eruption of Mount St. Helens, B. Volcanol., 78, 30, https://doi.org/10.1007/s00445-016-1024-5, 2016.

Gonnermann, H. M. and Manga, M.: The fluid mechanics inside a volcano, Annu. Rev. Fluid Mech., 39, 321–356, 2007.

Goto, A.: A new model for volcanic earthquake at Unzen Volcano: Melt rupture model, Geophys. Res. Lett., 26, 2541–2544, 1999.

Goto, A., Fukui, K., Hiraga, T., Nishida, Y., Ishibashi, H., Matsushima, T., Miyamoto, T., and Sasaki, O.: Rigid migration of Unzen lava rather than flow, J. Volcanol. Geoth. Res., 407, 107073, https://doi.org/10.1016/j.jvolgeores.2020.107073, 2020.

Hale, A. J. and Wadge, G.: The transition from endogenous to exogenous growth of lava domes with the development of shear bands, J. Volcanol. Geoth. Res., 171, 237–257, 2008.

Harnett, C. E., Kendrick, J. E., Lamur, A., Thomas, M. E., Stinton, A., Wallace, P. A., Utley, J. E. P., Murphy, W., Neuberg, J., and Lavallée, Y.: Evolution of Mechanical Properties of Lava Dome Rocks Across the 1995–2010 Eruption of Soufrière Hills Volcano, Montserrat, Front. Earth Sci., 7, 7, https://doi.org/10.3389/feart.2019.00007, 2019.

Heap, M. J. and Kennedy, B. M.: Exploring the scale-dependent permeability of fractured andesite, Earth Planet. Sc. Lett., 447, 139–150, https://doi.org/10.1016/j.epsl.2016.05.004, 2016.

Heap, M. J. and Violay, M. E. S.: The mechanical behaviour and failure modes of volcanic rocks: a review, B. Volcanol., 83, 33, https://doi.org/10.1007/s00445-021-01447-2, 2021.

Heap, M. J., Kolzenburg, S., Russell, J. K., Campbell, M. E., Welles, J., Farquharson, J. I., and Ryan, A.: Conditions and timescales for welding block-and-ash flow deposits, J. Volcanol. Geoth. Res., 289, 202–209, 2014.

Heap, M. J., Farquharson, J. I., Baud, P., Lavallée, Y., and Reuschle, T.: Fracture and compaction of andesite in a volcanic edifice, B. Volcanol., 77, 55, https://doi.org/10.1007/s00445-015-0938-7, 2015a.

Heap, M. J., Kennedy, B. M., Pernin, N., Jacquemard, L., Baud, P., Farquharson, J. I., Scheu, B., Lavallee, Y., Gilg, H. A., Letham-Brake, M., Mayer, K., Jolly, A. D., Reuschle, T., and Dingwell, D. B.: Mechanical behaviour and failure modes in the Whakaari (White Island volcano) hydrothermal system, New Zealand, J. Volcanol. Geoth. Res., 295, 26–42, https://doi.org/10.1016/j.jvolgeores.2015.02.012, 2015b.

Heap, M. J., Kennedy, B. M., Farquharson, J. I., Ashworth, J., Mayer, K., LEtham-Brake, M., Reuschlé, T., Gilg, H. A., Scheu, B., Lavallée, Y., Siratovich, P. A., Cole, J. W., Jolly, A. D., Baud, P., and Dingwell, D. B.: A multidisciplinary approach to quantify the permeability of the Whakaari/ White Island volcanic hydrothermal system (Taupo Volcanic Zone, New Zealand), J. Volcanol. Geoth. Res., 332, 88–108, https://doi.org/10.1016/j.jvolgeores.2016.12.004, 2017a.

Heap, M. J., Violay, M., Wadsworth, F. B., and Vasseur, J.: From rock to magma and back again: The evolution of temperature and deformation mechanism in conduit margin zones, Earth Planet. Sc. Lett., 463, 92–100, https://doi.org/10.1016/j.epsl.2017.01.021, 2017b.

Heap, M. J., Troll, V. R., Kushnir, A. R. L., Gilg, H. A., Collinson, A. S. D., Deegan, F. M., Darmawan, H., Seraphine, N., Neuberg, J., and Walter, T. R.: Hydrothermal alteration of andesitic lava domes can lead to explosive volcanic behaviour, Nat. Commun., 10, 5063, https://doi.org/10.1038/s41467-019-13102-8, 2019.

Heiken, G., Wohletz, K., and Eichelberger, J.: Fracture fillings and intrusive pyroclasts, Inyo domes, California, J. Geophys. Res.-Solid, 93, 4335–4350, https://doi.org/10.1029/JB093iB05p04335, 1988.

Holland, A. S. P., Watson, I. M., Phillips, J. C., Caricchi, L., and Dalton, M. P.: Degassing processes during lava dome growth: Insights from Santiaguito lava dome, Guatemala, J. Volcanol. Geoth. Res., 202, 153–166, https://doi.org/10.1016/j.jvolgeores.2011.02.004, 2011.

Holtz, F., Sato, H., Lewis, J., Behrens, H., and Nakada, S.: Experimental petrology of the 1991–1995 Unzen dacite, Japan. Part I: Phase relations, phase composition and pre-eruptive conditions, J. Petrol., 46, 319–337, https://doi.org/10.1093/petrology/egh077, 2005.

Hornby, A. J., Kendrick, J. E., Lamb, O. D., Hirose, T., De Angelis, S., von Aulock, F. W., Umakoshi, K., Miwa, T., Henton De Angelis, S., Wadsworth, F. B., Hess, K.-U., Dingwell, D. B., and Lavallée, Y.: Spine growth and seismogenic faulting at Mt. Unzen, Japan, J. Geophys. Res.-Sol. Ea., 120, 2169–9356, https://doi.org/10.1002/2014JB011660, 2015.

Hornby, A. J., Lavallée, Y., Kendrick, J. E., De Angelis, S., Lamur, A., Rietbrock, A., and Chigna, G.: Brittle-ductile deformation and tensile rupture of dome lava during inflation at Santiaguito, Guatemala, J. Geophys. Res.-Sol. Ea., 124, 10107–10131, https://doi.org/10.1029/2018JB017253, 2019.

Jaupart, C. and Allègre, C. J.: Gas content, eruption rate and instabilities or eruption regime in silicic volcanoes, Earth Planet. Sc. Lett., 102, 413–429, https://doi.org/10.1016/0012-821x(91)90032-d, 1991.

Kendrick, J. E., Lavallée, Y., Ferk, A., Perugini, D., Leonhardt, R., and Dingwell, D. B.: Extreme frictional processes in the volcanic conduit of Mount St. Helens (USA) during the 2004–2008 eruption, J. Struct. Geol., 38, 61–76, https://doi.org/10.1016/j.jsg.2011.10.003, 2012.

Kendrick, J. E., Lavallée, Y., Hess, K. U., Heap, M. J., Gaunt, H. E., Meredith, P. G., and Dingwell, D. B.: Tracking the permeable porous network during strain-dependent magmatic flow, J. Volcanol. Geoth. Res., 260, 117–126, https://doi.org/10.1016/j.jvolgeores.2013.05.012, 2013.

Kendrick, J. E., Lavallée, Y., Hess, K.-U., De Angelis, S., Ferk, A., Gaunt, H. E., Meredith, P. G., Dingwell, D. B., and Leonhardt, R.: Seismogenic frictional melting in the magmatic column, Solid Earth, 5, 199–208, https://doi.org/10.5194/se-5-199-2014, 2014a.

Kendrick, J. E., Lavallée, Y., Hirose, T., Di Toro, G., Hornby, A. J., De Angelis, S., and Dingwell, D. B.: Volcanic drumbeat seismicity caused by stick-slip motion and magmatic frictional melting, Nat. Geosci., 7, 438–442, https://doi.org/10.1038/ngeo2146, 2014b.

Kendrick, J. E., Lavallée, Y., Varley, N. R., Wadsworth, F. B., Lamb, O. D., and Vasseur, J.: Blowing off steam: Tuffisite formation as a regulator for lava dome eruptions, Front. Earth Sci., 4, 41, https://doi.org/10.3389/feart.2016.00041, 2016.

Kendrick, J. E., Schaefer, L. N., Schauroth, J., Bell, A. F., Lamb, O. D., Lamur, A., Miwa, T., Coats, R., Lavallée, Y., and Kennedy, B. M.: Physical and mechanical rock properties of a heterogeneous volcano: the case of Mount Unzen, Japan, Solid Earth, 12, 633–664, https://doi.org/10.5194/se-12-633-2021, 2021.

Kennedy, B. M., Wadsworth, F. B., Vasseur, J., Schipper, C. I., Jellinek, A. M., von Aulock, F. W., Hess, K. U., Russell, J. K., Lavallee, Y., Nichols, A. R. L., and Dingwell, D. B.: Surface tension driven processes densify and retain permeability in magma and lava, Earth Planet. Sc. Lett., 433, 116–124, https://doi.org/10.1016/j.epsl.2015.10.031, 2016.

Kennedy, L. A. and Russell, J. K.: Cataclastic production of volcanic ash at Mount Saint Helens, Phys. Chem. Earth, 45–46, 40–49, https://doi.org/10.1016/j.pce.2011.07.052, 2012.

Klug, C. and Cashman, K. V.: Permeability development in vesiculating magmas: Implications for fragmentation, B. Volcanol., 58, 87–100, https://doi.org/10.1007/s004450050128, 1996.

Kolzenburg, S., Heap, M. J., Lavallée, Y., Russell, J. K., Meredith, P. G., and Dingwell, D. B.: Strength and permeability recovery of tuffisite-bearing andesite, Solid Earth, 3, 191–198, https://doi.org/10.5194/se-3-191-2012, 2012.

Kueppers, U., Scheu, B., Spieler, O., and Dingwell, D. B.: Field-based density measurements as tool to identify preeruption dome structure: set-up and first results from Unzen volcano, Japan, J. Volcanol. Geoth. Res., 141, 65–75, 2005.

Kusakabe, M., Sato, H., Nakada, S., and Kitamura, T.: Water contents and hydrogen isotopic ratios of rocks and minerals from the 1991 eruption of Unzen volcano, Japan, J. Volcanol. Geoth. Res., 89, 231–242, https://doi.org/10.1016/s0377-0273(98)00134-6, 1999.

Kushnir, A. R. L., Martel, C., Bourdier, J. L., Heap, M. J., Reuschle, T., Erdmann, S., Komorowski, J. C., and Cholik, N.: Probing permeability and microstructure: Unravelling the role of a low-permeability dome on the explosivity of Merapi (Indonesia), J. Volcanol. Geoth. Res., 316, 56–71, https://doi.org/10.1016/j.jvolgeores.2016.02.012, 2016.

Kushnir, A. R. L., Martel, C., Champallier, R., and Arbaret, L.: In situ confirmation of permeability development in shearing bubble-bearing melts and implications for volcanic outgassing, Earth Planet. Sc. Lett., 458, 315–326, https://doi.org/10.1016/j.epsl.2016.10.053, 2017a.

Kushnir, A. R. L., Martel, C., Champallier, R., and Wadsworth, F. B.: Permeability Evolution in Variably Glassy Basaltic Andesites Measured Under Magmatic Conditions, Geophys. Res. Lett., 44, 10262–10271, https://doi.org/10.1002/2017gl074042, 2017b.

Lamb, O. D., De Angelis, S., Umakoshi, K., Hornby, A. J., Kendrick, J. E., and Lavallée, Y.: Repetitive fracturing during spine extrusion at Unzen volcano, Japan, Solid Earth, 6, 1277–1293, https://doi.org/10.5194/se-6-1277-2015, 2015.

Lamur, A., Kendrick, J. E., Eggertsson, G. H., Wall, R. J., Ashworth, J. D., and Lavallée, Y.: The permeability of fractured rocks in pressurised volcanic and geothermal systems, Sci. Rep.-UK, 7, 6173, https://doi.org/10.1038/s41598-017-05460-4, 2017.

Lamur, A., Kendrick, J. E., Wadsworth, F. B., and Lavallée, Y.: Fracture healing and strength recovery in magmatic liquids, Geology, 47, 195–198, https://doi.org/10.1130/g45512.1, 2019.

Laumonier, M., Arbaret, L., Burgisser, A., and Champallier, R.: Porosity redistribution enhanced by strain localization in crystal-rich magmas, Geology, 39, 715–718, https://doi.org/10.1130/g31803.1, 2011.

Lavallée, Y. and Kendrick, J. E.: A review of the physical and mechanical properties of volcanic rocks and magmas in the brittle and ductile regimes, in: Forecasting and planning for volcanic hazards, risks, and disasters, Vol. 2, 2nd Edn., edited by: Papale, P., Elsevier, https://doi.org/10.1016/B978-0-12-818082-2.00005-6, 2020.

Lavallée, Y. and Kendrick, J. E.: Strain localisation in magmas, in: Magmas, Melts, Liquids and Glasses: Experimental Insights, edited by: Neuville, D. R., Henderson, G. S., and Dingwell, D. B., Reviews in Minerlogy and Geochemistry, Mineralogical Society of America, Vol. 87, Geological Melts, ISBN 978-1-946850-08-9, 2021.

Lavallée, Y., Hess, K.-U., Cordonnier, B., and Dingwell, D. B.: Non-Newtonian rheological law for highly crystalline dome lavas, Geology, 35, 843–846, https://doi.org/10.1130/g23594a.1, 2007.

Lavallée, Y., Meredith, P. G., Dingwell, D. B., Hess, K. U., Wassermann, J., Cordonnier, B., Gerik, A., and Kruhl, J. H.: Seismogenic lavas and explosive eruption forecasting, Nature, 453, 507–510, https://doi.org/10.1038/nature06980, 2008.

Lavallée, Y., Varley, N. R., Alatorre-Ibargueengoitia, M. A., Hess, K. U., Kueppers, U., Mueller, S., Richard, D., Scheu, B., Spieler, O., and Dingwell, D. B.: Magmatic architecture of dome-building eruptions at Volcan de Colima, Mexico, B. Volcanol., 74, 249–260, https://doi.org/10.1007/s00445-011-0518-4, 2012.

Lavallée, Y., Benson, P. M., Heap, M. J., Hess, K.-U., Flaws, A., Schillinger, B., Meredith, P. G., and Dingwell, D. B.: Reconstructing magma failure and the degassing network of dome-building eruptions, Geology, 41, 515–518, https://doi.org/10.1130/g33948.1, 2013.

Lavallée, Y., Dingwell, D. B., Johnson, J. B., Cimarelli, C., Hornby, A. J., Kendrick, J. E., von Aulock, F. W., Kennedy, B. M., Andrews, B. J., Wadsworth, F. B., Rhodes, E., and Chigna, G.: Thermal vesiculation during volcanic eruptions, Nature, 528, 544–547, https://doi.org/10.1038/nature16153, 2015.

Lejeune, A. M. and Richet, P.: Rheology of Crystal-Bearing Silicate Melts – an Experimental-Study at High Viscosities, J. Geophys. Res.-Sol. Ea., 100, 4215–4229, 1995.

Lejeune, A. M., Bottinga, Y., Trull, T. W., and Richet, P.: Rheology of bubble-bearing magmas, Earth Planet. Sc. Lett., 166, 71–84, 1999.

Liu, Y., Zhang, Y. X., and Behrens, H.: Solubility of H_2O in rhyolitic melts at low pressures and a new empirical model for mixed H_2O-CO_2 solubility in rhyolitic melts, J. Volcanol. Geoth. Res., 143, 219–235, https://doi.org/10.1016/j.jvolgeores.2004.09.019, 2005.

Loaiza, S., Fortin, J., Schubnel, A., Gueguen, Y., Vinciguerra, S., and Moreira, M.: Mechanical behavior and localized failure modes in a porous basalt from the Azores, Geophys. Res. Lett., 39, L19304, https://doi.org/10.1029/2012gl053218, 2012.

Mader, H. M., Llewellin, E. W., and Mueller, S. P.: The rheology of two-phase magmas: A review and analysis, J. Volcanol. Geoth. Res., 257, 135–158, https://doi.org/10.1016/j.jvolgeores.2013.02.014, 2013.

Matoza, R. S. and Chouet, B. A.: Subevents of long-period seismicity: Implications for hydrothermal dynamics during the 2004–2008 eruption of Mount St. Helens, J. Geophys. Res.-Sol. Ea., 115, B12206, https://doi.org/10.1029/2010jb007839, 2010.

Melnik, O. and Sparks, R. S. J.: Nonlinear dynamics of lava dome extrusion, Nature, 402, 37–41, 1999.

Michaut, C., Ricard, Y., Bercovici, D., and Sparks, R. S. J.: Eruption cyclicity at silicic volcanoes potentially caused by magmatic gas waves, Nat. Geosci., 6, 856–860, https://doi.org/10.1038/ngeo1928, 2013.

Mueller, S., Melnik, O., Spieler, O., Scheu, B., and Dingwell, D. B.: Permeability and degassing of dome lavas undergoing rapid decompression: An experimental determination, B. Volcanol., 67, 526–538, 2005.

Mueller, S., Scheu, B., Spieler, O., and Dingwell, D. B.: Permeability control on magma fragmentation, Geology, 36, 399–402, https://doi.org/10.1130/g24605a.1, 2008.

Nakada, S. and Motomura, Y.: Petrology of the 1991–1995 eruption at Unzen: effusion pulsation and groundmass crystallization, J. Volcanol. Geoth. Res., 89, 173–196, https://doi.org/10.1016/s0377-0273(98)00131-0, 1999.

Nakada, S., Miyake, Y., Sato, H., Oshima, O., and Fujinawa, A.: Endogenous growth of dacite dome at Unzen volcano (Japan), 1993–1994, Geology, 23, 157–160, https://doi.org/10.1130/0091-7613(1995)023<0157:egodda>2.3.co;2, 1995.

Nakada, S., Shimizu, H., and Ohta, K.: Overview of the 1990–1995 eruption at Unzen Volcano, J. Volcanol. Geoth. Res., 89, 1–22, https://doi.org/10.1016/s0377-0273(98)00118-8, 1999.

Navon, O., Chekhmir, A., and Lyakhovsky, V.: Bubble growth in highly viscous melts: theory, experiments, and autoexplosivity of dome lavas, Earth Planet. Sc. Lett., 160, 763–776, https://doi.org/10.1016/s0012-821x(98)00126-5, 1998.

Neuberg, J. W., Tuffen, H., Collier, L., Green, D., Powell, T., and Dingwell, D.: The trigger mechanism of low-frequency earthquakes on Montserrat, J. Volcanol. Geoth. Res., 153, 37–50, 2006.

Newhall, C. G. and Melson, W. G.: Explosive activity associated with the growth of volcanic domes, J. Volcanol. Geoth. Res., 17, 111–131, https://doi.org/10.1016/0377-0273(83)90064-1, 1983.

Ohba, T., Hirabayashi, J.-I., Nogami, K., Kusakabe, M., and Yoshida, M.: Magma degassing process during the eruption of Mt. Unzen, Japan in 1991 to 1995: Modeling with the chemical composition of volcanic gas, J. Volcanol. Geoth. Res., 175, 120–132, https://doi.org/10.1016/j.jvolgeores.2008.03.040, 2008.

Okumura, S. and Sasaki, O.: Permeability reduction of fractured rhyolite in volcanic conduits and its control on eruption cyclicity, Geology, 42, 843–846, https://doi.org/10.1130/g35855.1, 2014.

Okumura, S., Nakamura, M., and Tsuchiyama, A.: Shear-induced bubble coalescence in rhyolitic melts with low vesicularity, Geophys. Res. Lett., 33, L20316, https://doi.org/10.1029/2006gl027347, 2006.

Okumura, S., Nakamura, M., Tsuchiyama, A., Nakano, T., and Uesugi, K.: Evolution of bubble microstructure in sheared rhyolite: Formation of a channel-like bubble network, J. Geophys. Res.-Sol. Ea., 113, B07208, https://doi.org/10.1029/2007jb005362, 2008.

Okumura, S., Nakamura, M., Takeuchi, S., Tsuchiyama, A., Nakano, T., and Uesugi, K.: Magma deformation may induce non-explosive volcanism via degassing through bubble networks, Earth Planet. Sc. Lett., 281, 267–274, https://doi.org/10.1016/j.epsl.2009.02.036, 2009.

Okumura, S., Nakamura, M., Nakano, T., Uesugi, K., and Tsuchiyama, A.: Shear deformation experiments on vesicular rhyolite: Implications for brittle fracturing, degassing, and compaction of magmas in volcanic conduits, J. Geophysi. Res.-Sol. Ea., 115, B06201, https://doi.org/10.1029/2009jb006904, 2010.

Okumura, S., Nakamura, M., Nakano, T., Uesugi, K., and Tsuchiyama, A.: Experimental constraints on permeable gas transport in crystalline silicic magmas, Contrib. Mineral. Petr., 164, 493–504, https://doi.org/10.1007/s00410-012-0750-8, 2012.

Okumura, S., Nakamura, M., Uesugi, K., Nakano, T., and Fujioka, T.: Coupled effect of magma degassing and rheology on silicic volcanism, Earth Planet. Sc. Lett., 362, 163–170, https://doi.org/10.1016/j.epsl.2012.11.056, 2013.

Pallister, J. S., Cashman, K. V., Hagstrum, J. T., Beeler, N. M., Moran, S. C., and Denlinger, R. P.: Faulting within the Mount St. Helens conduit and implications for volcanic earthquakes, Geol. Soc. Am. Bull., 125, 359–376, https://doi.org/10.1130/b30716.1, 2013a.

Pallister, J. S., Diefenbach, A. K., Burton, W. C., Muñoz, J., Griswold, J. P., Lara, L. E., Lowernster, J. B., and Valenzuela, C. E.: The Chaitén rhyolite lava dome: Eruption sequence, lava dome volumes, rapid effusion rates and source of the rhyolite magma, Andean Geol., 40, 277–294, 2013b.

Paterson, M. S. and Wong, T.-F.: Experimental Rock Deformation – The Brittle Field, Science-Technology, 347 pp., https://doi.org/10.1007/3-540-26339-X_1, 2005.

Pistone, M., Caricchi, L., Ulmer, P., Burlini, L., Ardia, P., Reusser, E., Marone, F., and Arbaret, L.: Deformation experiments of bubble- and crystal-bearing magmas: Rheological and microstructural analysis, J. Geophys. Res.-Sol. Ea., 117, B05208, https://doi.org/10.1029/2011jb008986, 2012.

Platz, T., Cronin, S. J., Procter, J. N., Neal, V. E., and Foley, S. F.: Non-explosive, dome-forming eruptions at Mt. Taranaki, New Zealand, Geomorphology, 136, 15–30, https://doi.org/10.1016/j.geomorph.2011.06.016, 2012.

Radon, J.: On the determination of functions from their integral values along certain manifolds, IEEE T. Med. Imaging, 5, 170–176, https://doi.org/10.1109/tmi.1986.4307775, 1986.

Ramsay, J. G.: Shear zone geometry: A review, J. Struct. Geol., 2, 83–99, https://doi.org/10.1016/0191-8141(80)90038-3, 1980.

Rhodes, E., Kennedy, B. M., Lavallée, Y., Hornby, A., Edwards, M., and Chigna, G.: Textural Insights Into the Evolving Lava Dome Cycles at Santiaguito Lava Dome, Guatemala, Front. Earth Sci., 6, 30, https://doi.org/10.3389/feart.2018.00030, 2018.

Rohnacher, A., Rietbrock, A., Gottschämmer, E., Carter, W., Lavallée, Y., De Angelis, S., Kendrick, J. E., and Chigna, G.: Source mechanism of seismic explosion signals at Santiaguito volcano, Guatemala: New insights from seismic analysis and numerical modeling, Front. Earth Sci., 8, 603441, https://doi.org/10.3389/feart.2020.603441, 2021.

Rust, A. C. and Cashman, K. V.: Permeability of vesicular silicic magma: inertial and hysteresis effects, Earth Planet. Sc. Lett., 228, 93–107, 2004.

Rust, A. C. and Cashman, K. V.: Permeability controls on expansion and size distributions of pyroclasts, J. Geophys. Res.-Sol. Ea., 116, B11202, https://doi.org/10.1029/2011jb008494, 2011.

Rust, A. C. and Manga, M.: Bubble shapes and Orientations in low Re simple shear flow, J. Colloid Interf. Sci., 249, 476–480, https://doi.org/10.1006/jcis.2002.8292, 2002.

Rust, A. C., Manga, M., and Cashman, K. V.: Determining flow type, shear rate and shear stress in magmas from bubble shapes and orientations, J. Volcanol. Geoth. Res., 122, 111–132, 2003.

Rutter, E. H.: On the nomenclature of mode of failure transitions in rocks, Tectonophysics, 122, 381–387, https://doi.org/10.1016/0040-1951(86)90153-8, 1986.

Ryan, A. G., Heap, M. J., Russell, J. K., Kennedy, L. A., and Clynne, M. A.: Cyclic shear zone cataclasis and sintering during lava dome extrusion: Insights from Chaos Crags, Lassen Volcanic Center (USA), J. Volcanol. Geoth. Res., 401, 106935, https://doi.org/10.1016/j.jvolgeores.2020.106935, 2020.

Sahagian, D.: Volcanology – Magma fragmentation in eruptions, Nature, 402, 589–591, 1999.

Sahetapy-Engel, S. T. and Harris, A. J. L.: Thermal structure and heat loss at the summit crater of an active lava dome, B. Volcanol., 71, 15–28, https://doi.org/10.1007/s00445-008-0204-3, 2009.

Sato, H., Suto, S., Ui, T., Fujii, T., Yamamoto, T., Takarada, S., and Sakaguchi, K.: Flowage of the 1991 Unzen lava; discussions to Goto et al., 2020 "Rigid migration of Unzen lava rather than flow" J. Volcanol. Geotherm. Res.,

110, 107073, J. Volcanol. Geoth. Res., 420, 107343, https://doi.org/10.1016/j.jvolgeores.2021.107343, 2021.

Saubin, E., Kennedy, B., Tuffen, H., Villeneuve, M. C., Davidson, J., and Burchardt, S.: Comparative field study of shallow rhyolite intrusions in Iceland: Emplacement mechanisms and impact on country rocks, J. Volcanol. Geoth. Res., 388, 106691, https://doi.org/10.1016/j.jvolgeores.2019.106691, 2019.

Schaefer, L. N., Kennedy, B. M., Kendrick, J. E., Lavallée, Y., and Miwa, T.: Laboratory Measurements of Damage Evolution in Dynamic Volcanic Environments: From Slow to Rapid Strain Events, 54th U.S. Rock Mechanics/Geomechanics Symposium, ARMA-2020-1876, ISBN 978-0-9794975-5-1, 2020.

Scheu, B., Spieler, O., and Dingwell, D. B.: Dynamics of explosive volcanism at Unzen volcano: an experimental contribution, B. Volcanol., 69, 175–187, 2006.

Scheu, B., Kueppers, U., Mueller, S., Spieler, O., and Dingwell, D. B.: Experimental volcanology on eruptive products of Unzen, J. Volcanol. Geoth. Res., 175, 110–119, https://doi.org/10.1016/j.jvolgeores.2008.03.023, 2007.

Shields, J. K., Mader, H. M., Pistone, M., Caricchi, L., Floess, D., and Putlitz, B.: Strain-induced outgassing of three-phase magmas during simple shear, J. Geophys. Res.-Sol. Ea., 119, 6936–6957, https://doi.org/10.1002/2014jb011111, 2014.

Smith, J. V.: Structural analysis of flow-related textures in lavas, Earth-Sci. Rev., 57, 279–297, https://doi.org/10.1016/s0012-8252(01)00081-2, 2002.

Smith, J. V., Miyake, Y., and Oikawa, T.: Interpretation of porosity in dacite lava domes as ductile-brittle failure textures, J. Volcanol. Geoth. Res., 112, 25–35, https://doi.org/10.1016/s0377-0273(01)00232-3, 2001.

Sparks, R. S. J.: Causes and consequences of pressurisation in lava dome eruptions, Earth Planet. Sc. Lett., 150, 177–189, 1997.

Sparks, R. S. J.: Dynamics of magma degassing, Geol. Soc. Lond. Spec. Publ., 213, 5–22, https://doi.org/10.1144/GSL.SP.2003.213.01.02, 2003.

Sparks, R. S. J., Murphy, M. D., Lejeune, A. M., Watts, R. B., Barclay, J., and Young, S. R.: Control on the emplacement of the andesite lava dome of the Soufriere Hills volcano, Montserrat by degassing-induced crystallization, Terra Nova, 12, 14–20, 2000.

Stasiuk, M. V., Barclay, J., Carroll, M. R., Jaupart, C., Ratte, J. C., Sparks, R. S. J., and Tait, S. R.: Degassing during magma ascent in the Mule Creek vent (USA), B. Volcanol., 58, 117–130, 1996.

Stix, J., Layne, G. D., and Williams, S. N.: Mechanisms of degassing at Nevado del Ruiz volcano, Colombia, J. Geol. Soc., 160, 507–521, 2003.

Tait, S., Jaupart, C., and Vergniolle, S.: Pressure, gas content and eruption periodicity of a shallow, crystallizing magma chamber, Earth Planet. Sc. Lett., 92, 107–123, https://doi.org/10.1016/0012-821x(89)90025-3, 1989.

Thomas, M. E. and Neuberg, J.: What makes a volcano tick – A first explanation of deep multiple seismic sources in ascending magma, Geology, 40, 351–354, https://doi.org/10.1130/G32868.1, 2012.

Tiab, D. and Donaldson, E. C.: Chapter 3 – Porosity and Permeability, in: Petrophysics, 4th Edn., edited by: Tiab, D. and Donaldson, E. C., Gulf Professional Publishing, Boston, 67–186, 2016.

Tuffen, H. and Dingwell, D. B.: Fault textures in volcanic conduits: evidence for seismic trigger mechanisms during silicic eruptions, B. Volcanol., 67, 370–387, 2005.

Tuffen, H., Dingwell, D. B., and Pinkerton, H.: Repeated fracture and healing of silicic magma generate flow banding and earthquakes?, Geology, 31, 1089–1092, 2003.

Umakoshi, K., Takamura, N., Shinzato, N., Uchida, K., Matsuwo, N., and Shimizu, H.: Seismicity associated with the 1991–1995 dome growth at Unzen Volcano, Japan, J. Volcanol. Geoth. Res., 175, 91–99, https://doi.org/10.1016/j.jvolgeores.2008.03.030, 2008.

Varley, N. R. and Taran, Y.: Degassing processes of popocatepetl and Volcan de Colima, Mexico, in: Volcanic Degassing, edited by: Oppenheimer, C. P. D. M. B. J., Geological Society Special Publication, 263–280, 2003.

Vasseur, J., Wadsworth, F. B., Lavallée, Y., Hess, K.-U., and Dingwell, D. B.: Volcanic sintering: Timescales of viscous densification and strength recovery, Geophys. Res. Lett., 40, 5658–5664, https://doi.org/10.1002/2013gl058105, 2013.

Venezky, D. Y. and Rutherford, M. J.: Petrology and Fe-Ti oxide reequilibration of the 1991 Mount Unzen mixed magma, J. Volcanol. Geoth. Res., 89, 213–230, https://doi.org/10.1016/s0377-0273(98)00133-4, 1999.

Wadsworth, F. B., Vasseur, J., von Aulock, F. W., Hess, K.-U., Scheu, B., Lavallée, Y., and Dingwell, D. B.: Nonisothermal viscous sintering of volcanic ash, J. Geophys. Res.-Sol. Ea., 119, 8792–8804, https://doi.org/10.1002/2014jb011453, 2014.

Wadsworth, F. B., Vasseur, J., Scheu, B., Kendrick, J. E., Lavallée, Y., and Dingwell, D. B.: Universal scaling of fluid permeability during volcanic welding and sediment diagenesis, Geology, 44, 219–222, https://doi.org/10.1130/g37559.1, 2016.

Wadsworth, F. B., Vasseur, J., Llewellin, E. W., Dobson, K. J., Colombier, M., von Aulock, F. W., Fife, J. L., Wiesmaier, S., Hess, K.-U., Scheu, B., Lavallée, Y., and Dingwell, D. B.: Topological inversions in coalescing granular media control fluid-flow regimes, Phys. Rev. E, 96, 033113, https://doi.org/10.1103/PhysRevE.96.033113, 2017.

Wadsworth, F. B., Witcher, T., Vossen, C. E. J., Hess, K.-U., Unwin, H. E., Scheu, B., Castro, J. M., and Dingwell, D. B.: Combined effusive-explosive silicic volcanism straddles the multiphase viscous-to-brittle transition, Nat. Commun., 9, 4696, https://doi.org/10.1038/s41467-018-07187-w, 2018.

Wadsworth, F. B., Witcher, T., Vasseur, J., Dingwell, D. B., and Scheu, B.: When Does Magma Break?, in: Volcanic Unrest: From Science to Society, edited by: Gottsmann, J., Neuberg, J., and Scheu, B., Advances in Volcanology, 171–184, 2019.

Wadsworth, F. B., Vasseur, J., Llewellin, E. W., Brown, R. J., Tuffen, H., Gardner, J. E., Kendrick, J. E., Lavallée, Y., Dobson, K. J., Heap, M. J., Dingwell, D. B., Hess, K.-U., Schauroth, J., von Aulock, F. W., Kushnir, A. R. L., and Marone, F.: A model for permeability evolution during volcanic welding, J. Volcanol. Geoth. Res., 409, 107118, https://doi.org/10.1016/j.jvolgeores.2020.107118, 2021.

Wallace, P. A., Kendrick, J. E., Ashworth, J. D., Miwa, T., Coats, R., De Angelis, S. H., Mariani, E., Utley, J. E. P., Biggin, A., Kendrick, R., Nakada, S., Matsushima, T., and Lavallée, Y.: Petrological architecture of a magmatic shear zone: A multidisciplinary investigation of strain localisation during magma ascent at Unzen Volcano, Japan, J. Petrol., 60, 791–826, https://doi.org/10.1093/petrology/egz016, 2019.

Watanabe, T., Shimizu, Y., Noguchi, S., and Nakada, S.: Permeability measurements on rock samples from Unzen scientific drilling

project drill hole 4 (USDP-4), J. Volcanol. Geoth. Res., 175, 82–90, https://doi.org/10.1016/j.jvolgeores.2008.03.021, 2008.

Watts, R. B., Herd, R. A., Sparks, R. S. J., and Young, S. R.: Growth patterns and emplacement of the andesitic lava dome at Soufriere Hills Volcano, Montserrat, in: Eruption of Soufriere Hills Volcano, Montserrat, from 1995 to 1999, edited by: Druitt, T. H. and Kokelaar, P., 21, Geological Society of London Memoir, 115–152, 2002.

Westrich, H. R. and Eichelberger, J. C.: Gas transport and bubble collapse in rhyolitic magma – an experimental approach, B. Volcanol., 56, 447–458, https://doi.org/10.1007/bf00302826, 1994.

Woods, A. W. and Koyaguchi, T.: Transitions between explosive and effusive eruptions of silicic magmas, Nature, 370, 641–644, 1994.

Wright, H. M. N. and Weinberg, R. F.: Strain localization in vesicular magma: Implications for rheology and fragmentation, Geology, 37, 1023–1026, https://doi.org/10.1130/g30199a.1, 2009.

Wright, H. M. N., Roberts, J. J., and Cashman, K. V.: Permeability of anisotropic tube pumice: Model calculations and measurements, Geophys. Res. Lett., 33, L17316, https://doi.org/10.1029/2006gl027224, 2006.

Yamasato, H.: Nature of infrasonic pulse accompanying low frequency earthquake at Unzen volcano, Japan, Bulletin of the volcanological society of Japan, 43, 1–13, https://doi.org/10.18940/kazan.43.1_1, 1998.

Yamashina, K., Matsushima, T., and Ohmi, S.: Volcanic deformation at Unzen, Japan, visualized by a time-differential stereoscopy, J. Volcanol. Geoth. Res., 89, 73–80, https://doi.org/10.1016/s0377-0273(98)00124-3, 1999.

Yilmaz, T. I., Wadsworth, F. B., Gilg, H. A., Hess, K. U., Kendrick, J. E., Wallace, P. A., Lavallée, Y., Utley, J. E. P., Vasseur, J., Nakada, S., and Dingwell, D. B.: Rapid alteration of fractured volcanic conduits beneath Mt Unzen, B. Volcanol., 83, 34, https://doi.org/10.1007/s00445-021-01450-7, 2021.

Yoshimura, S. and Nakamura, M.: Fracture healing in a magma: An experimental approach and implications for volcanic seismicity and degassing, J. Geophys. Res.-Sol. Ea., 115, B09209, https://doi.org/10.1029/2009jb000834, 2010.

Zhang, Y. X.: H_2O in rhyolitic glasses and melts: Measurement, speciation, solubility, and diffusion, Rev. Geophys., 37, 493–516, 1999.